nature physics

Supplementary information

https://doi.org/10.1038/s41567-026-03383-4

Time-resolved imaging of antiferromagnetic skyrmion interactions

In the format provided by the authors and unedited

Contents

1 Section A1: Magnetic characterization and additional imaging

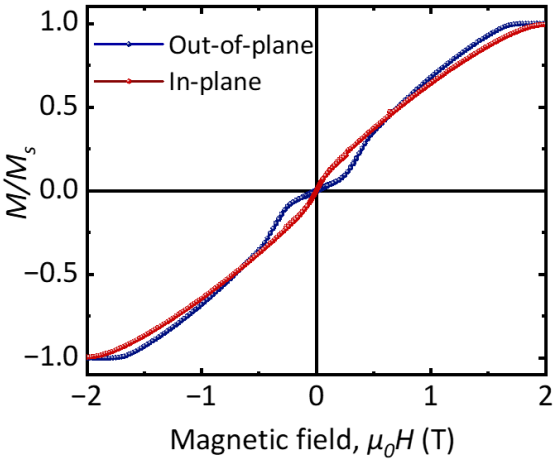

Figure S1. Magnetic hysteresis loops of the stack, showing out-of-plane and in-plane magnetization curves.

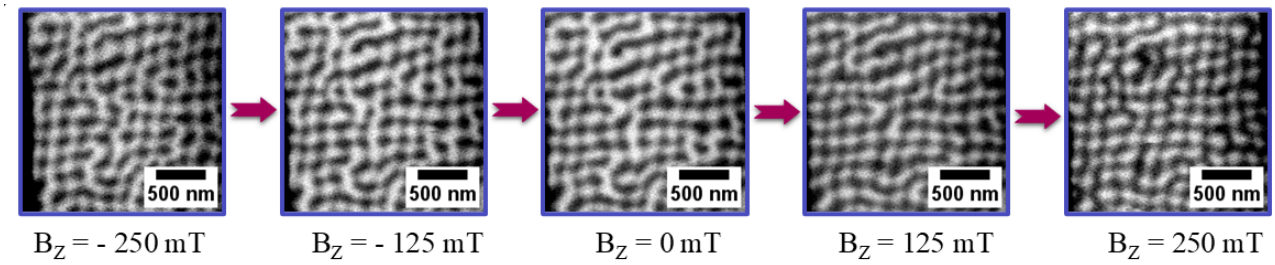

Figure S2. Field stability of the AFM skyrmion lattice. STXM images of the AFM skyrmion lattice recorded at the Co L_3 absorption edge under varying out-of-plane magnetic fields. The lattice remains stable across a wide field range, indicating robust magnetic ordering and resilience against external perturbations. Images correspond to applied fields of -250 mT, -125 mT, 0 mT, $+125$ mT, and $+250$ mT (left to right). The persistence of the skyrmion lattice over both polarities confirms the field stability of the antiferromagnetically coupled configuration in the fully compensated SyAFM stack.

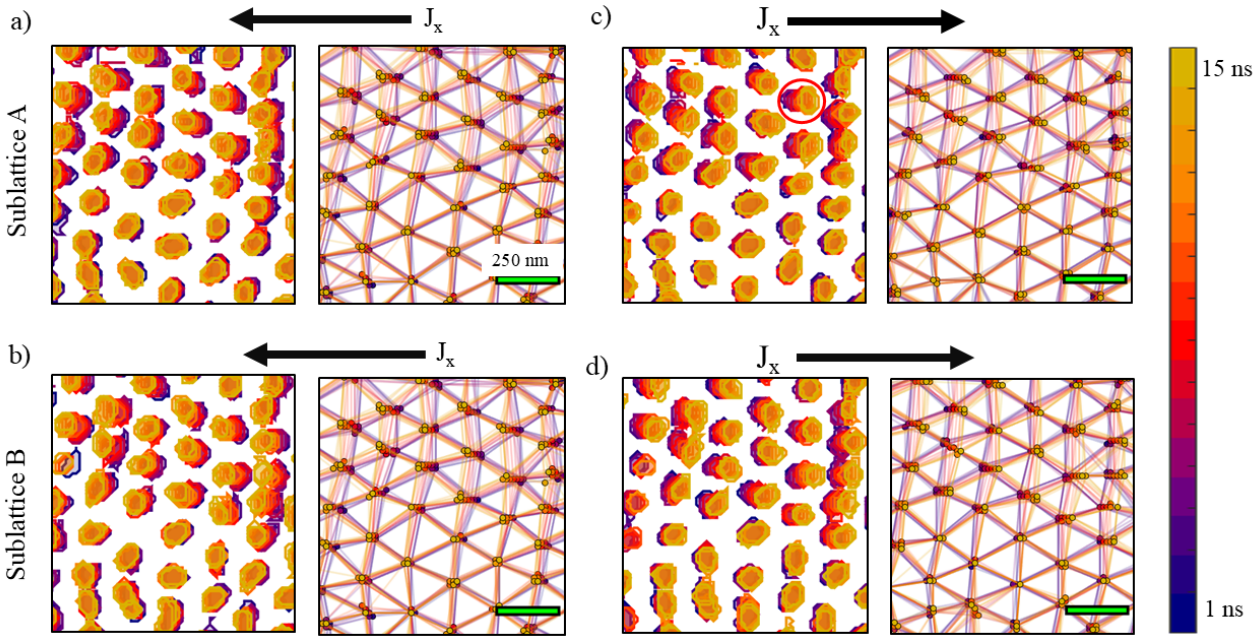

Figure S3. Incoherent flow regime of AFM skyrmion dynamics. (a) and **(b)** show the motion of skyrmions in sublattices A and B, respectively, under a positive current (J_x) with time evolution tracked over 15 ns. The skyrmion domain boundaries are color-coded to represent the time progression, from purple (earlier times) to yellow (later times). **(c)** and **(d)** illustrate the skyrmion behaviour at sublattices A and B, respectively, but under a reversed current direction ($-J_x$), demonstrating symmetric displacement and deformation, confirming sublattice coupling and effective SkHE compensation. The time scale for the evolution is indicated by the color bar on the right. The scale bar indicates 250 nm.

Detailed classification of skyrmions based on their trajectories

Table 1. Relaxation time constants τ_{relax} and amplitudes for different skyrmion classes after positive and negative current polarities of the bipolar cycle.

Skyrmion class	After -J_x		After +J_x	
	τ_{relax} (ns)	Amplitude (nm)	τ_{relax} (ns)	Amplitude (nm)
M	9.9	12.8	5.1	9.1
I	5.6	17.5	7.8	20.1
L	9.6	19.2	3.9	18.9
R	7.4	21.7	18.9	22.7

All skyrmion trajectories were analyzed based on their time-resolved displacement under bipolar current excitation. The classification is implemented from the trajectory shapes, rather than from the displacement map shown in Fig. 2(a). Specifically, three qualitatively distinct dynamical responses are observed. (i) Immobile skyrmions, which are strongly affected by pinning, exhibit no major displacement during the current pulse and importantly exhibit the same behaviour for both current pulse polarities. These are classified as class I. (ii) Mobile skyrmions, which are not significantly influenced by pinning, translate smoothly during the pulse and exhibit no significant relaxation effects; they also exhibit the same behaviour for both current polarities (moving with the same speed – just in opposite directions) and these are classified as class M. The distinct behaviour of these two classes is shown in Figure S4(a), where their average displacement

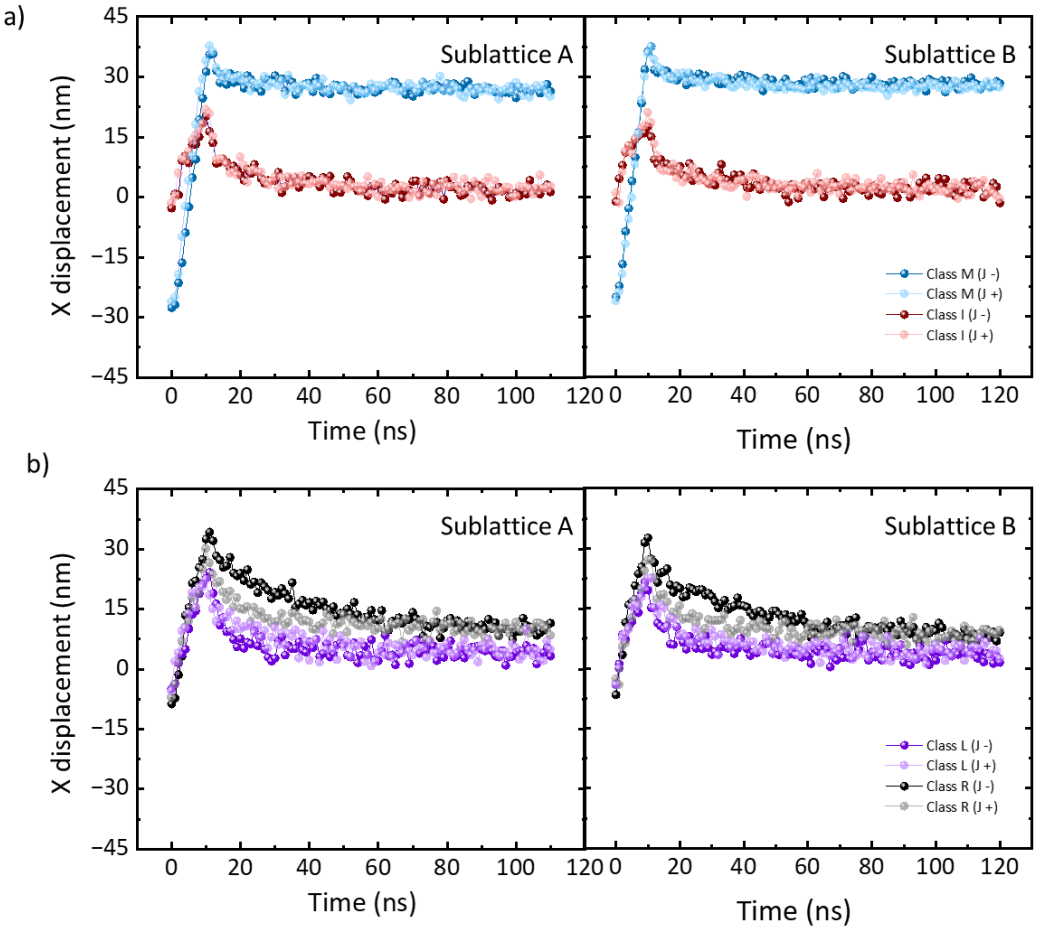

Figure S4. Sublattice-resolved recoil dynamics of distinct AFM skyrmion classes under bipolar current excitation. **(a, b)** Average displacement traces of skyrmion classes in sublattices A and B. **(a)** Immobile (I) and mobile (M) skyrmions, showing pronounced, nearly symmetric recoil. **(b)** Boundary skyrmions (L and R), defined by their spatial position relative to the mobile skyrmion region, exhibit asymmetric recoil dynamics with respect to current polarity. The time axis is aligned such that the arrival of the current pulse corresponds to $t = 0$ for both polarities. No temporal delay or phase shift is observed between the two sublattices for any skyrmion class.

traces exhibit the same dynamics for both current polarities (light blue and dark blue traces overlap and light red and dark red traces overlap identically). In addition, we observe a third type of trajectory with intermediate displacement but qualitatively different dynamics. As shown in Figure S4(b), these skyrmions exhibit strongly asymmetric deformation and relaxation dynamics with respect to current polarity (the grey and black traces do not overlap and the light purple and dark purple traces do not overlap for the full trace but they differ significantly). These skyrmions are spatially located at the boundary between the mobile and immobile skyrmion regions. We therefore classify them based on their spatial position relative to the class I skyrmions, defining two subclasses: L (left) and R (right). Importantly, these classes are not distinguished by displacement magnitude, but by their geometric location within the lattice, which gives rise to their characteristic asymmetric response with respect to the current polarity.

Supplementary Figure S5 presents time-resolved skyrmion trajectories as a function of current density for a 7.5 ns

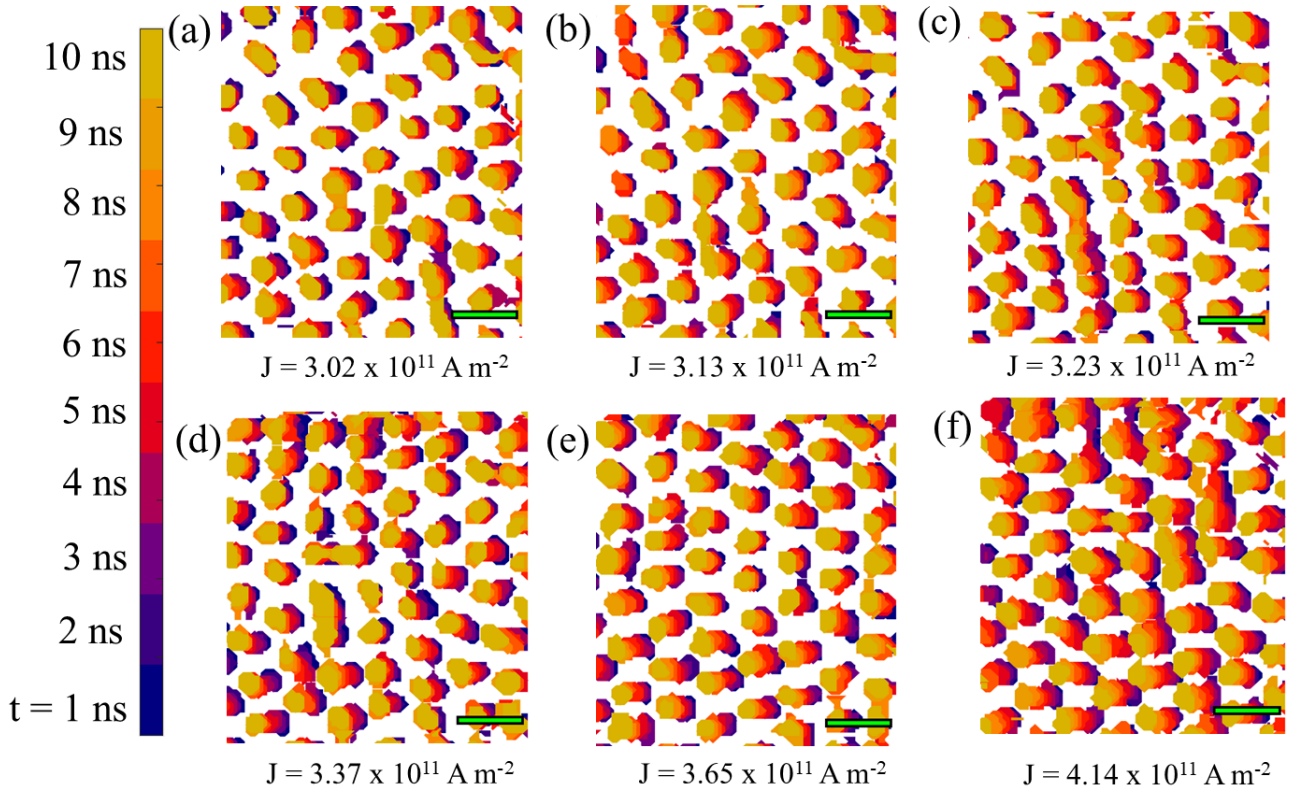

Figure S5. AFM skyrmion dynamics from incoherent to coherent flow regime of motion. (a–c) At lower current densities ($J = 3.02 - 3.23 \times 10^{11}$ A/m^2), skyrmion motion remains irregular due to pinning effects, leading to local lattice distortions and strain accumulation. **(d–f)** As the current density increases beyond $J = 3.37 \times 10^{11}$ A/m^2, the applied spin-orbit torque overcomes pinning barriers, enabling skyrmions to move coherently. This transition reduces lattice distortions and results in more uniform skyrmion trajectories. At the highest current density ($J = 4.14 \times 10^{11}$ A/m^2), the skyrmion lattice exhibits highly ordered motion with minimal deformation, marking the onset of a fully developed flow regime. The scale bar represents 250 nm.

pulse, revealing a transition from localized, heterogeneous motion to fully coherent flow. At lower currents (a–c), the spin–orbit torque is insufficient to fully overcome pinning, resulting in irregular and fragmented motion. As the current increases (see Figure S5(d–f)), skyrmions undergo a depinning transition and begin to move collectively with synchronized trajectories, maintaining local lattice order. This dynamic crossover reflects an effective flattening of the energy landscape, enabling uniform and deterministic transport.

2 Section A2: Structural characterization

Cross-sectional scanning transmission electron microscopy (STEM) in high-angle annular dark-field (HAADF) mode was performed to evaluate the structural quality of the SyAFM multilayer stack (Figure S6(a)). An electron-transparent cross-sectional lamella was prepared in a Thermo Fisher Scientific Helios dual-beam focused ion beam/scanning electron microscope (FIB–SEM) using a 30 kV Ga ion beam. The ion beam energy was decreased to 5 kV for the final thinning steps. STEM was carried out using a 300 kV TFS Spectra TEM equipped with a CEOS probe aberration corrector,

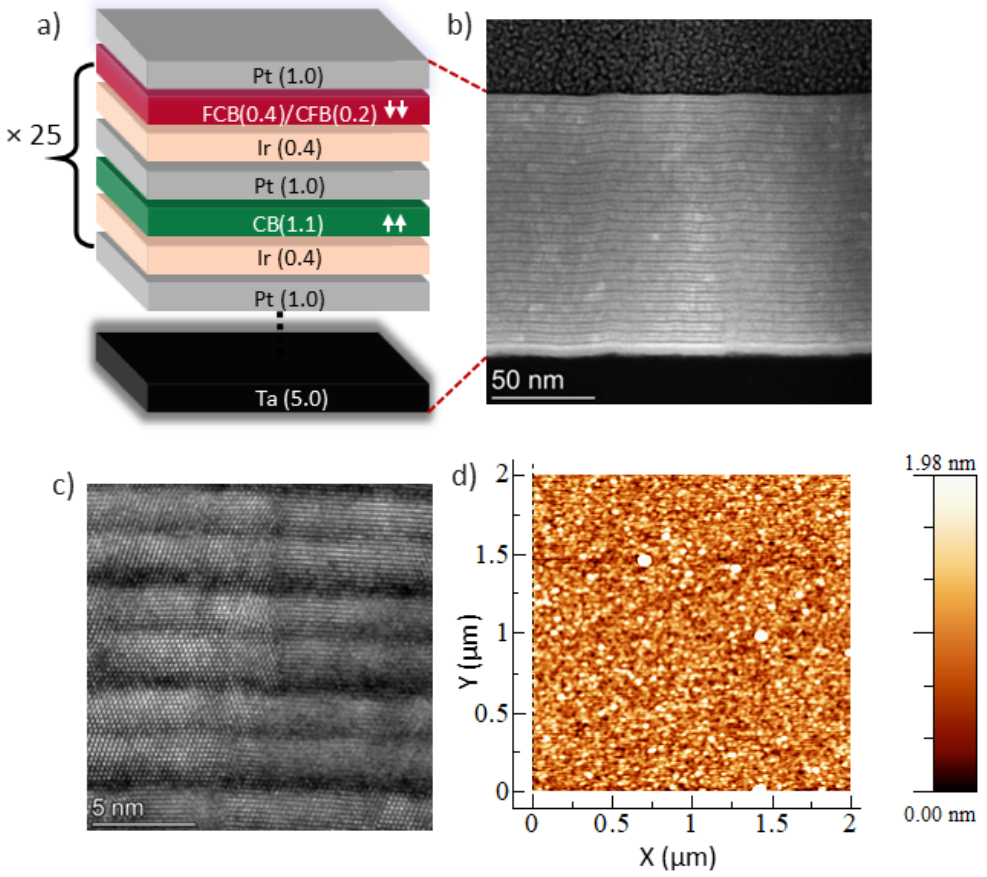

Figure S6. Structural characterization of the SyAFM multilayer stack. (a) Schematic of the SyAFM unit cell, repeated 25 times. **(b)** Cross-sectional STEM overview image showing continuous multilayer stacking with well-resolved periodic contrast across the full film thickness. **(c)** High-resolution STEM image revealing polycrystalline columnar grains and vertically correlated interface waviness. **(d)** Atomic force microscopy topography of the film surface, indicating homogeneous surface morphology.

a HAADF, and a Super-X EDX detection system. The overview STEM image (Figure S6(b)) shows 25 repetitions of the SyAFM unit cell with clearly resolved periodic contrast across the full film thickness. The multilayer is continuous, and no structural discontinuities or shorts between adjacent SyAFM blocks are observed. A high-resolution image (Figure S6(c)) reveals a polycrystalline columnar grain structure and a slight, vertically correlated interface waviness propagating throughout the stack. Topography analysis by atomic force microscopy (Figure S6(d)) shows a homogeneous surface morphology with an RMS roughness of 0.34 nm (2 μm $\times$ 2 μm scan, first-order plane subtraction). Considering the ultrathin nature of the magnetic and spacer layers, such nanoscale thickness and interface variations can be expected to locally modulate the interlayer exchange coupling, perpendicular anisotropy, and interfacial Dzyaloshinskii–Moriya interaction. Such spatial fluctuations provide a natural static microstructural landscape that can give rise to localized skyrmion pinning.

High-angle annular dark-field (HAADF) scanning transmission electron microscopy combined with energy-dispersive X-ray spectroscopy (EDX) was performed at the same cross-sectional position to examine the chemical integrity of

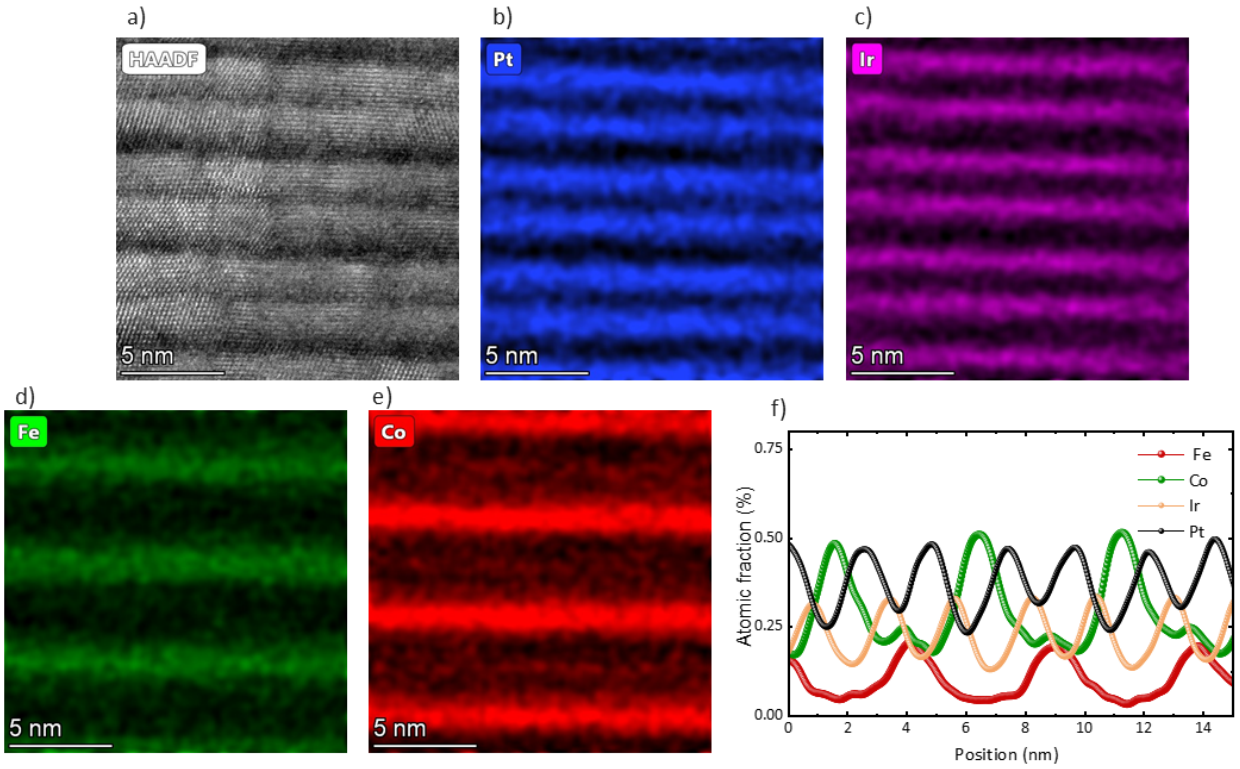

Figure S7. HAADF-STEM and EDX analysis of the SyAFM multilayer. (a) High-angle annular dark-field (HAADF) scanning transmission electron microscopy image acquired at a representative cross-sectional position (scale bar: 5 nm). **(b–e)** Corresponding element-resolved energy-dispersive X-ray spectroscopy (EDX) maps for Pt (b), Ir (c), Fe (d), and Co (e), showing spatially separated layers consistent with the nominal stacking sequence. **(f)** Relative elemental line profile extracted from the mapped region, displaying periodic modulation of elemental concentrations across successive SyAFM unit cells.

the multilayer stack (Figure S7). The HAADF image exhibits periodic contrast consistent with the designed multilayer architecture. Element-resolved EDX maps for Pt (Figure S7(b)), Ir (Figure S7(c)), Fe (Figure S7(d)), and Co (Figure S7(e)) reveal spatially separated layers in agreement with the nominal stacking sequence. The Fe- and Co-rich ferromagnetic layers are resolved as distinct sublayers, while the Pt and Ir spacer layers remain continuous across the stack. The corresponding compositional line profile (Figure S7(f)) shows periodic modulation of the elemental concentrations without evidence of large-scale intermixing, compositional segregation, or impurity clustering within the experimental resolution.

3 Section A3: Comparison with single skyrmion dynamics

The dynamics of an isolated skyrmion are conventionally classified into pinned, creep, and viscous flow regimes, determined by the competition between external driving forces and the local pinning landscape, including thermal activation[1,2]. In this dilute limit, each skyrmion depins independently, and the motion is governed predominantly by the local energy landscape without collective contributions from skyrmion-skyrmion interactions. While single AFM skyrmion dynamics have been studied using quasi-static imaging[3–5], direct pump-probe time-resolved measurements of isolated AFM skyrmions, to our knowledge, are experimentally unexplored.

In the fully compensated SyAFM stack used in the main text, the combination of negative domain-wall energy and strong interlayer antiferromagnetic coupling stabilizes an AFM skyrmion lattice over the accessible magnetic field range of -250 to $+250$ mT (the maximum field available during in-situ measurements at the STXM set-up). As a result, the system remains in a dense lattice configuration throughout this field range (Figure S2), preventing access to an isolated single-skyrmion regime within this fully compensated type of sample.

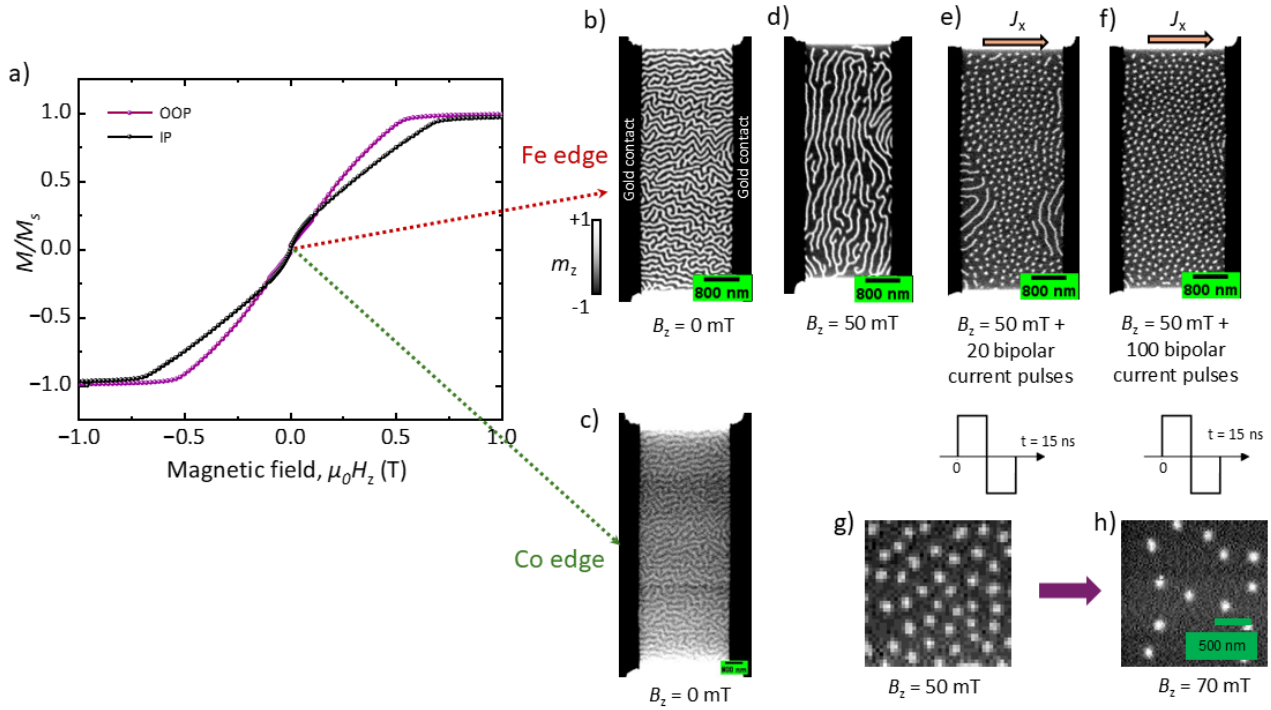

Figure S8. Field-controlled skyrmion nucleation and density tuning in a partially compensated SyAFM. (a) Out-of-plane (OOP) and in-plane (IP) hysteresis loops measured using SQUID, indicating reduced interlayer exchange coupling compared to the fully compensated stack used in the main text. **(b,c)** Element-selective magnetic imaging at zero magnetic field ($B_z = 0$ mT) at the Fe and Co edges, demonstrating antiferromagnetic coupling between the two sublattices and a multidomain labyrinth configuration. **(d)** Application of $B_z = 50$ mT. **(e,f)** Injection of bipolar current pulses (7.5 ns duration, $J \approx 2 \times 10^{12}$ A/m^2) fragments stripe domains and leads to the formation of skyrmions, resulting in a skyrmion lattice. **(g,h)** Increasing the OOP field from $B_z = 50$ mT to $B_z = 70$ mT significantly reduces the skyrmion density, yielding a configuration with increased inter-skyrmion spacing and strongly reduced interactions.

To establish an experimental comparison between collective lattice dynamics and single-skyrmion behavior, we fabricated a partially compensated SyAFM stack (approximately 90% magnetic compensation). The FM_{A} layer consists of FCB(0.35)/CFB(0.375), and FM_{B} consists of CB(0.4)/Ta(0.06)/CB(0.35)/Ta(0.06)/CB(0.35). The thicknesses are in nm. In contrast to the fully compensated stack discussed in the main text, the Pt spacer thickness was increased to 1.2 nm to reduce the interlayer exchange coupling strength, resulting in a lower saturation field, as shown in Figure S8(a). The system stabilizes in a multidomain labyrinth configuration due to the negative domain-wall energy of the stack, as evidenced from the zero remanence of the SQUID measurements. Element-selective imaging at zero magnetic field confirms antiferromagnetic coupling between the two sublattices (Fe edge for FM_{A} and Co edge for FM_{B}), as shown in Figure S8(b,c).

To realize current-driven dynamics studies, thermally assisted reproducible skyrmion nucleation was achieved using bipolar current-pulse injection in patterned nanowire devices with integrated gold contacts. In the absence of an external magnetic field, the film exhibits a disordered stripe domain state (Figure S8(b)). Applying a moderate out-of-plane field ($B_z = 50$ mT) reduces the average domain size (Figure S8(d)). The apparent elongation and partial alignment of the stripe domains is not a direct consequence of the applied out-of-plane field, but rather arises from a small residual in-plane field of approximately 1-2 mT originating from the quadrupole magnet during the measurements. Injection of bipolar current pulses (7.5 ns duration, $J \approx 2 \times 10^{12}$ A/m^2) fragments the stripe domains and leads to the formation of individual skyrmions (Figure S8(e,f)). The nucleation mechanism is governed primarily by transient Joule heating, which locally reduces the effective perpendicular anisotropy and lowers the energy barrier between stripe and skyrmion states[6,7]. Importantly, this sample enables tuning of the skyrmion density via the external magnetic field. Increasing the field from $B_z = 50$ mT to $B_z = 70$ mT significantly decreases the skyrmion density (Figure S8(g,h)), yielding a dilute configuration in which the average inter-skyrmion distance substantially exceeds the skyrmion diameter. In this dilute regime, skyrmion–skyrmion interaction effects are strongly reduced, and the measured dynamics predominantly reflect local pinning effects. This configuration, therefore, provides a direct experimental reference for distinguishing collective lattice dynamics from individual single skyrmion motion.

Time-resolved pump–probe measurements were performed on the isolated skyrmions under pulse conditions comparable to those used for the lattice measurements. We focus on a current density $J_x = 1.4 \times 10^{12}$ A/m^2 with a pulse width of 2.5 ns (see Supplementary Movie 4), for which the spin–orbit torque is comparable to the local pinning potential. We find that in this regime, the dynamics are governed primarily by spatial variations of the non-flat energy landscape. The initial configuration is shown in Figure S9(a), and the time-resolved x- and y-displacements are plotted in Figure S9(b,c). Under application of the bipolar pulse, skyrmion E remains effectively pinned, exhibiting negligible displacement, while skyrmions A, B, C, and D undergo finite motion along the current direction. The absence of motion of skyrmion E indicates that the applied current density remains below its individual depinning threshold, whereas the remaining skyrmions depin independently. Importantly, skyrmion A, located closest to the pinned skyrmion E, does not exhibit any measurable deviation from the average trajectory of skyrmions B, C, and D. The overlap of their displacement curves within experimental uncertainty indicates that the motion for the skyrmion distances observed is dominated by local pinning rather than interaction-mediated collective effects.

These results demonstrate that, for a single skyrmion, skyrmion dynamics reduce to independent depinning events determined by the local energy landscape, as here also observed in SyAFM. Accordingly, individual skyrmions exhibit either pinned behavior or viscous-flow motion with identical velocities once depinned. This behavior contrasts with the incoherent flow regime observed in the dense lattice, where elastic coupling between neighboring skyrmions gives rise to correlated distortions and collective recoil with different velocities depending on the skyrmion position. These measurements, therefore, provide an experimental reference for distinguishing pinning-dominated single-skyrmion motion

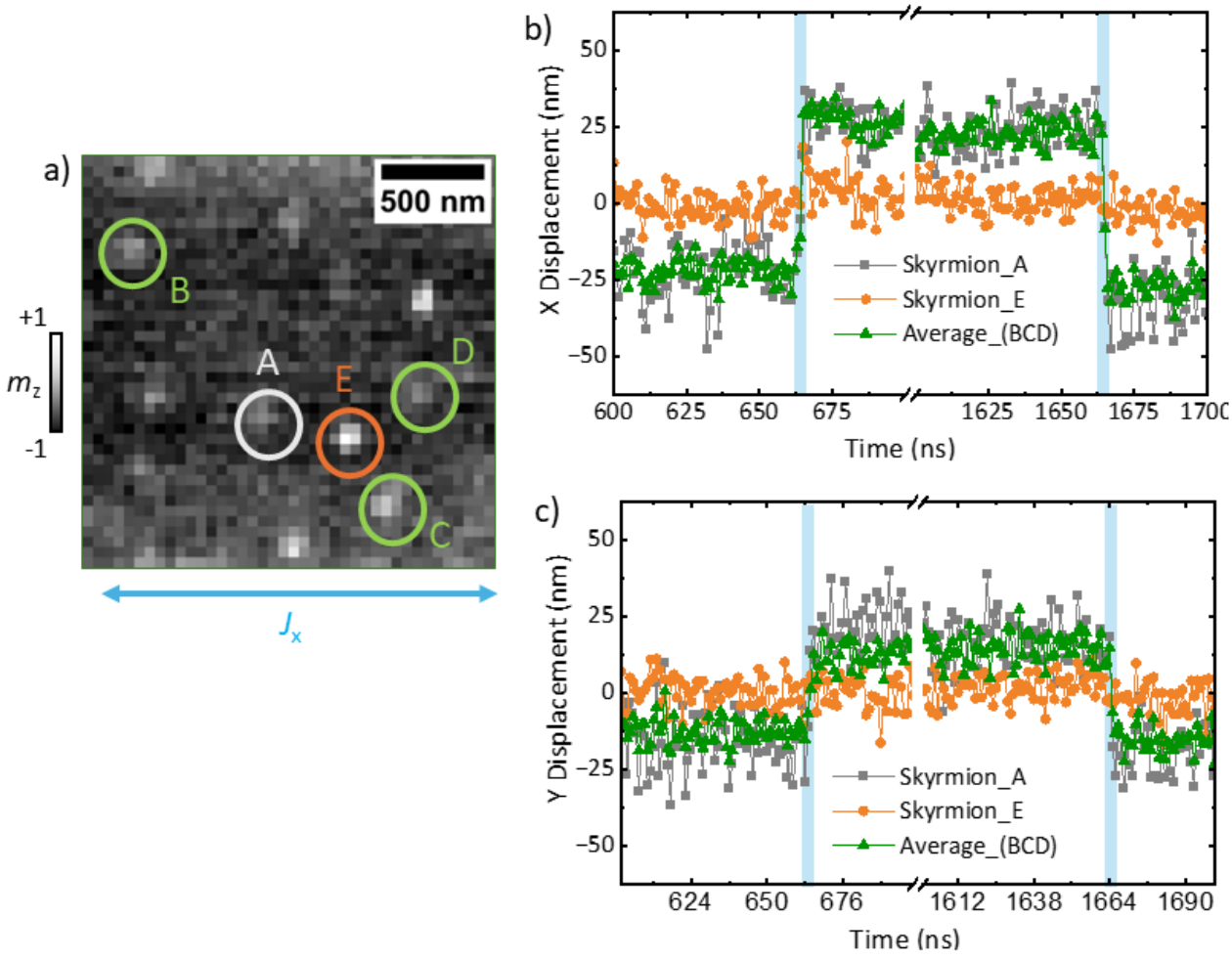

Figure S9. Time-resolved dynamics of isolated AFM skyrmions in a partially compensated SyAFM. (a) STXM image at $B_z = 70$ mT showing spatially separated skyrmions (labels A–E). The current direction (J_x) is indicated. **(b,c)** Time-resolved longitudinal (x) and transverse (y) displacements under bipolar current pulses ($J_x = 1.4 \times 10^{12}$ A/m^2, 2.5 ns pulse width). Skyrmion E remains pinned, while skyrmions A, B, C, and D exhibit finite motion.

from interaction-driven lattice dynamics. Note that here, the skyrmions exhibit finite displacements along both the longitudinal (x) and transverse (y) directions. The presence of a measurable transverse component reflects a residual skyrmion Hall effect arising from the ∼90% magnetic compensation of the SyAFM stack.

We note that a distinct creep regime cannot be resolved with our pump–probe time-resolved approach. Creep motion is inherently stochastic and non-reproducible from cycle to cycle. As a result, the pump–probe scheme, which selectively captures only reproducible dynamics, averages out such stochastic motion, preventing direct observation of creep in time-resolved measurements. In this case, the stochastic nature of the motion leads to a smeared signal in our time-resolved images. We therefore do not resolve a distinct creep regime in our experiments.

4 Section A4: Role of Joule heating in skyrmion dynamics

To quantify the role of Joule heating, we performed temperature calibration measurements[8,9]. First, the device resistance was measured as a function of temperature, yielding a linear dependence with a temperature coefficient of $(0.026 \pm 2.35 \times 10^{-4})\ \Omega\,\mathrm{K}^{-1}$ (Figure S10(a)). This calibration enables conversion of transient resistance changes into an effective temperature rise. Using this calibration, we extract the temperature increase ΔT as a function of applied voltage under pulsed excitation. For a pulse width of $7\ \mathrm{ns}$, we obtain a temperature rise of up to $\sim 90\ \mathrm{K}$ at an applied voltage of $11.5\ \mathrm{V}$, corresponding to a current density of $1.2 \times 10^{12}\ \mathrm{A\,m^{-2}}$ (Figure S10(b)).

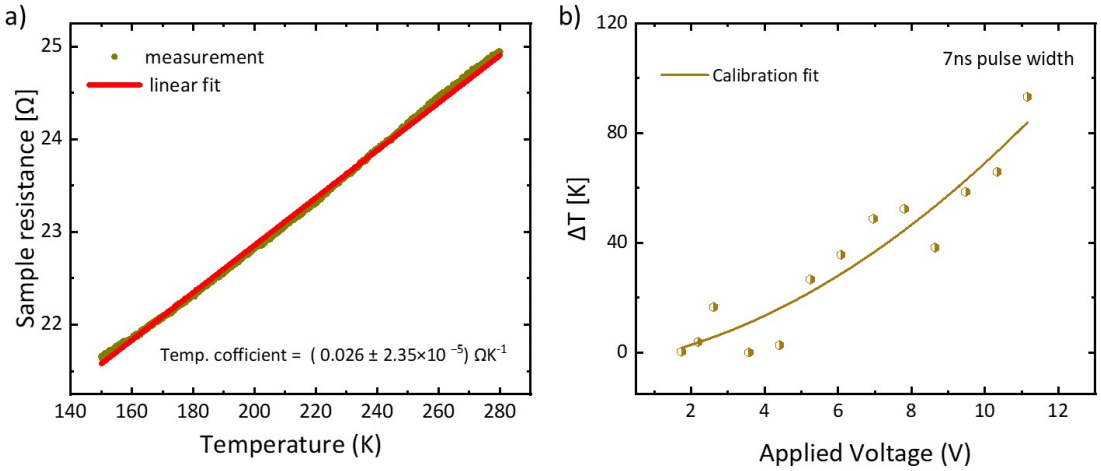

Figure S10. Joule heating calibration and temperature estimation. (a) Temperature-dependent resistance of the device, showing a linear dependence used to extract the temperature coefficient. **(b)** Extracted temperature rise Δ T as a function of applied voltage under pulsed excitation (7 ns pulse width), obtained from the resistance calibration. The solid line shows the calibration fit.

To estimate the temperature increase under the experimental conditions used for the dynamics measurements, we account for the shorter pulse duration of $2.5\ \mathrm{ns}$. In the regime where heat diffusion during the pulse is limited, the temperature rise scales approximately linearly with the pulse duration. Therefore, reducing the pulse width from $7\ \mathrm{ns}$ to $2.5\ \mathrm{ns}$ yields an estimated temperature increase of $\Delta T \approx 32\ \mathrm{K}$ at the same applied voltage.

To assess whether the estimated temperature rise qualitatively alters the magnetic properties of the SyAFM stack, we performed temperature-dependent SQUID magnetometry measurements at $330\ \mathrm{K}$ and $360\ \mathrm{K}$ (Figure S11), including both out-of-plane and in-plane hysteresis loops. With increasing temperature, the effective anisotropy decreases as the system approaches the spin reorientation transition (SRT). However, in the experimentally relevant range (300–330 K), the system remains in the perpendicular regime with a positive effective anisotropy ($K_{\mathrm{eff}} \approx 0.04\ \mathrm{MJ\,m^{-3}}$ at $330\ \mathrm{K}$), indicating that the SRT is not crossed. Most importantly, the interlayer antiferromagnetic exchange remains robust and continues to dominate the saturation field. The reduction in K_{eff} primarily affects the domain wall energy and leads to a modest increase in the domain wall width. However, given that the variation of K_{eff} within the 300–$330\ \mathrm{K}$ range is small, the

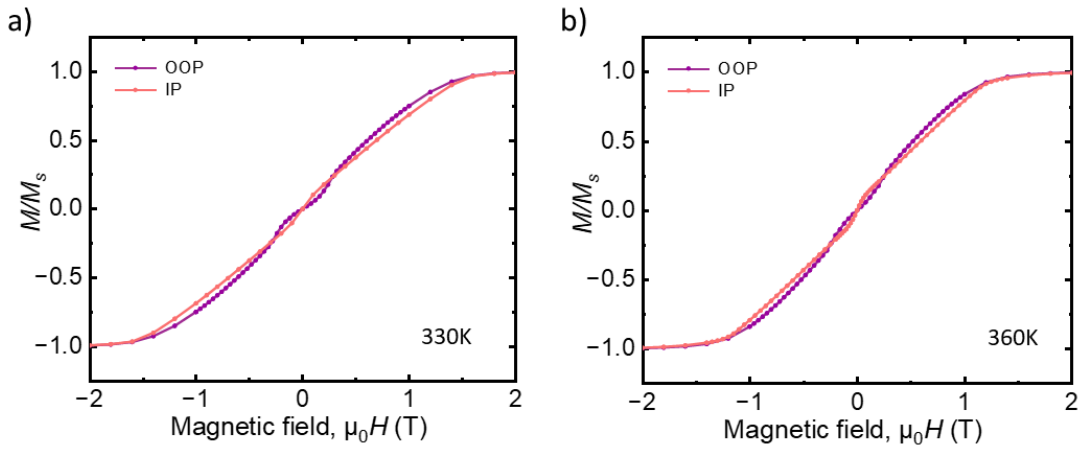

Figure S11. Temperature-dependent magnetic hysteresis loops. Out-of-plane (OOP) and in-plane (IP) magnetization curves at (a) 330K and (b) 360K.

corresponding change in domain wall properties is limited. Consistently, we do not observe any significant modification of the energy landscape or any measurable change in skyrmion size under these conditions in the STXM measurements.

The transient temperature rise during the current pulse can temporarily soften the effective local pinning landscape and thereby reduce effective depinning barriers. Joule heating may therefore assist skyrmion motion during the pulse. However, it cannot account for the main features of the observed dynamics. In particular, the skyrmion motion reverses upon reversing the current polarity (Fig. 4(c,d) in the main text), whereas Joule heating is polarity-independent. The directional response therefore identifies spin–orbit torque as the driving mechanism. Moreover, the interaction potential is extracted from the post-pulse recoil, i.e. after the current is switched off, when no additional Joule heating is generated and the sample is already relaxing back toward equilibrium. The measured recoil thus reflects the intrinsic restoring forces set by skyrmion–skyrmion repulsion and the pinning landscape. Finally, because the pump–probe STXM signal is averaged over billions of identical cycles, stochastic thermally activated events do not contribute to the measured contrast. The observed trajectories therefore reflect deterministic, reproducible dynamics. Taken together, Joule heating may assist depinning during the pulse, but it does not dominate either the directional motion or the post-pulse relaxation dynamics that underlie our analysis as evidenced by the fully reproducible pump-probe dynamics.

5 Section B1: Inverse parameter estimation and uncertainty inference via the Thiele equation

In this first section, we outline in general terms the methodology employed to estimate the parameters of the skyrmion-skyrmion interaction potential and to infer the associated uncertainties. This procedural framework will subsequently be applied to both experimental and micromagnetic datasets in section 6. We begin by defining the force model that will be used throughout the remainder of this analysis, although we note that the methodology is, in principle, extensible to alternative force formulations and higher-dimensional parameter spaces. Following this, we delineate the observed trajectories into two disjoint subsets. The first subset comprises trajectories for which we aim to predict the dynamics by systematically varying the parameters, seeking optimal agreement with the empirical data in order to estimate the parameters. The second subset includes trajectories of skyrmions that are not directly subject to prediction but exert non-negligible interactions upon those trajectories we aim to predict. Subsequently, we specify the Thiele model which underlies our prediction, and describe in detail the numerical time integration scheme employed, including the initialization and adaptation of the starting configurations. On this foundation, we perform parameter estimation by comparing the predicted trajectories across varying parameter configurations with the observed data. Finally, we present the procedure by which uncertainties in the estimated parameters can be inferred.

5.1 Force

In the following coordinate system, the in-plane coordinates are defined as x and y. The skyrmion - skyrmion interaction, which we will primarily consider in the form of a force, is assumed to be radially symmetric and depends only on the relative displacement vector $\vec{r} = \vec{r}_1 - \vec{r}_2$. The resulting force acting on the skyrmion located at $\vec{r}_1$, due to another Skyrmion at $\vec{r}_2$, is given by

$$\vec{F}_{(a,b)}(\vec{r}) = \frac{\vec{r}}{|\vec{r}|} F_{(a,b)}(|\vec{r}|), \qquad \frac{F(r)}{D} = \frac{F_{(a,b)}(r)}{D} = 1\,\mathrm{m\,s^{-1}} \exp\left(-\frac{(r-b)}{a}\right), \tag{1}$$

where $r = |\vec{r}|$ is the distance between the two Skyrmions. The function $F(r)$ represents only the radial component of the interaction force. The parameter a characterizes the steepness and effective range of the force, while b determines the strength of the force. Here, D denotes the dissipation constant. From the study of scattering trajectories, it is possible to determine only the ratio $F_{(a,b)}(r)/D$. Since the prefactor $1\,\mathrm{m\,s^{-1}}$ is comparable in magnitude to the typical velocities of the system, the parameter b is likewise of the same order as the approximate effective interaction distance. Alternative functional forms for the force, other than the exponential, have been tested. However, the exponential form proved to be optimal for the method applied here. While it is possible to include more than two parameters, the restriction to just a and b suffices for the present discussion and simplifies the analysis. This functional form for skyrmion potentials has been used previously for different skyrmion systems[10,11].

The interaction potential $V = V_{(a,b)}(r)$, derived from $\vec{F}(\vec{r}) = -\nabla V$, is given with $|\vec{r}| = r$ by

$$V_{(a,b)}(|\vec{r}|) = V_{(a,b)}(r) = (1\,\mathrm{m\,s^{-1}})\,D a \exp\left(-\frac{r-b}{a}\right). \tag{2}$$

5.2 Classification of data

To determine the skyrmion–skyrmion force and corresponding potential, we use reference trajectories obtained from experiments or micromagnetic simulations. These data sets are the observed data.

We consider n_g sets of observed trajectories, denoted by O_g, where $g \in \{1, \ldots, n_g\}$. Each set O_g consists of a collection of trajectories within a specific spatial region of the system. For example, in the later case where we apply these methods with $n_g = 2$, O_1 denotes the set of trajectories describing the relaxation of skyrmions after a current in the direction $j_x > 0$ is applied and then switched off, while O_2 denotes the set of trajectories describing the relaxation of skyrmions after a current in the direction $j_x < 0$ is applied and then switched off. The individual trajectories within O_g are denoted by $\vec{r}_{O_g,i}(t)$, where i indexes the trajectory. Each set O_g is further divided into two subsets: the estimation subset E_g, which contains the trajectories of skyrmions for which we aim to estimate the interaction potential, and the boundary subset B_g, which contains trajectories of skyrmions that are not directly involved in the estimation process but nevertheless influence those in E_g, and are therefore referred to as boundary skyrmions. The respective trajectories are denoted as $\vec{r}_{E_g,i}(t)$ for the skyrmions in E_g, and $\vec{r}_{B_g,i}(t)$ for the skyrmions in B_g.

To estimate the skyrmion – skyrmion interaction potential characterized by the parameters a and b from the trajectories in O_g, we must compute and compare simulated trajectories. These simulated trajectories are denoted by P_g, where g again indexes the different trajectory sets. The individual trajectories within P_g are denoted by $\vec{r}_{P_g,i}(t)$. The set P_g is optimized to match the trajectories in E_g as closely as possible. The indexing is chosen such that $\vec{r}_{P_g,i}(t)$ is intended to approximate the corresponding reference trajectory $\vec{r}_{E_g,i}(t)$. When it is necessary to emphasize the dependence of the simulated trajectories on specific parameters a and b, we write $P_g(a,b)$ to indicate the set of trajectories generated using those specific parameters.

5.3 Thiele equation and trajectory calculation for a single parameterization

To compute the trajectories over the time interval from $t_{g,1}$ to $t_{g,2}$ for each set P_g, the Thiele equation is used as the underlying model. Specifically, we start with the following form of the Thiele equation for synthetic antiferromagnets[4,12,13]:

$$D\dot{\vec{r}}_{P_g(a,b),i} = \vec{F}_{\mathrm{tot.},(a,b)} = \sum_{\substack{j \\ \vec{r}_{P_g,j} \in P_g,\, j \neq i}} \vec{F}_{(a,b)}(\vec{r}_{P_g,i} - \vec{r}_{P_g,j}) + \sum_{\substack{j \\ \vec{r}_{B_g,j} \in B_g}} \vec{F}_{(a,b)}(\vec{r}_{P_g,i} - \vec{r}_{B_g,j}), \tag{3}$$

where $\dot{\vec{r}}_{P_g,i} = \dot{\vec{r}}_{P_g(a,b),i}$ denotes the time derivative of the trajectory $\vec{r}_{P_g,i}$, $\vec{F}_{\mathrm{tot.},(a,b)}$ is the total force acting on the respective skyrmion, and D is the dissipation constant. As can be seen, the boundary skyrmion trajectories in B_g, although not

directly part of the estimation process, are included in the force calculation, since these skyrmions influence the original trajectories in E_g. Therefore, they must be taken into account when computing the simulated trajectories P_g.

For the numerical time integration, the forward Euler method is used with a time step Δt, i.e.,

$$\vec{r}_{P_g(a,b),i}(t+\Delta t) = \vec{r}_{P_g(a,b),i}(t) + \frac{\Delta t}{D}\vec{F}_{\text{tot.},(a,b)}(t). \tag{4}$$

To ensure that the time integration is sufficiently accurate, smaller time steps than the original sampling intervals $t_{g,i+1} - t_{g,i}$ from the data set g are used. Since the boundary skyrmions B_g are required during integration, and their positions are only available at discrete time points, linear interpolation in time t is used between $\vec{r}_{B_g,i}(t_{g,i})$ and $\vec{r}_{B_g,i}(t_{g,i+1})$ to estimate the positions at intermediate time steps $t \in (t_{g,i}, t_{g,i+1})$, where no data is directly available.

To predict, for a given parameter pair (a,b), the trajectory that should fit with E_g – along with its associated boundary trajectories B_g – an initial condition is required. This initial condition is determined iteratively by repeated forward integration. The reason for this step is that the trajectories in E_g, which we aim to predict, are themselves subject to measurement errors, including uncertainty in their initial positions $\vec{r}_{E_g,i}(t_{g,1})$. If these initial values $\vec{r}_{E_g,i}(t_{g,1})$ are used directly, unphysical dynamics may occur at the beginning of the simulated trajectory due to a mismatch in the relative positions of the skyrmions.

To mitigate this issue, we initialize the iterative refinement process by setting the following initial and target endpoints in the first iteration ($q = 1$):

$$\vec{r}^{\,q=1}_{1,g,i} = \vec{r}_{E_g,i}(t_{g,1}), \qquad \vec{r}^{\,q=1}_{2,g,i} = \vec{r}_{E_g,i}(t_{g,2}). \tag{5}$$

With this, we compute the solution $\vec{r}^{\,q=1}_{P_g(a,b),i}(t)$ using the Euler integration scheme from Equation 4, with the initial condition defined as

$$\vec{r}^{\,q}_{P_g(a,b),i}(t_{g,1}) = \vec{r}^{\,q}_{1,g,i}. \tag{6}$$

The trajectory is integrated up to time $t_{g,2}$. In the subsequent iteration ($q = 2$), the initial and target endpoints are updated according to

$$\vec{r}^{\,q}_{1,g,i} = \vec{r}^{\,q-1}_{1,g,i} + \left(\vec{r}^{\,q-1}_{P_g(a,b),i}(t_{g,2}) - \vec{r}^{\,q-1}_{2,g,i}\right), \qquad \vec{r}^{\,q}_{2,g,i} = \vec{r}^{\,q-1}_{P_g(a,b),i}(t_{g,2}). \tag{7}$$

The difference vector $\vec{\delta} = \vec{r}^{\,q-1}_{P_g(a,b),i}(t_{g,2}) - \vec{r}^{\,q-1}_{2,g,i}$ serves as a measure of the error in the initial condition. Since the final position after integration is determined purely by the force-driven dynamics, it provides a more accurate indication of the skyrmion's true trajectory. The correction vector $\vec{\delta}$ is applied to the initial condition, effectively shifting it toward a configuration that yields more consistent dynamics relative to the measured trajectory. Using the updated initial condition

from Equation 6, the Euler integration is performed for the iteration $q = 2$. After integration, the new start and end points for iteration $q = 3$ are then redefined using Equation 7, and the process continues accordingly. This iterative procedure is repeated until approximate convergence is achieved, i.e., when the displacement $\vec{\delta}$ is sufficiently small and on the order of the error of E_g. The final, converged trajectory after $q = q_c$ iterations is then taken as the solution,

$$\vec{r}_{P_g(a,b),i}(t) = \vec{r}^{\,q=q_c}_{P_g(a,b),i}(t). \tag{8}$$

5.4 Inference of the parameters and their uncertainty

The predicted trajectories P_g are compared to the estimation trajectories E_g, which originate from experiments or micromagnetic simulations and are used to estimate–i.e., optimally determine–the parameters a and b of the interaction potential. For the comparison, a specific time interval from $t_{g,1}$ to $t_{g,2}$ is considered. To this end, we define a loss function $L_2(a,b)$, which depends on the force parameters and is given by

$$L_2(a,b) = \sum_{g=1}^{n_g} \frac{1}{n_{t,g}} \sum_{i=1}^{n_{t,g}} \sum_{e=1}^{n_{E_g}} \sum_{c\in\{x,y\}} \frac{\left((\vec{r}_{P_g(a,b),e}(t_{g,i}) - \vec{r}_{E_g,e}(t_{g,i}))_c \right)^2}{2\sigma^2}, \tag{9}$$

where the summation is taken over all trajectory sets g, over all time steps $t_{g,i}$ for which data are available in the interval $[t_{g,1}, t_{g,2}]$, over all skyrmions in the estimation subset E_g, and over both spatial components $c \in \{x,y\}$. Here, $\vec{r}_{P_g(a,b),e}(t)$ denotes the predicted trajectory for a given parameter pair (a,b), and $(\ldots)_c$ indicates the c-th Cartesian component of the vector. The quantity $n_{t,g}$ represents the number of time steps for which skyrmion positions are available in the g-th trajectory set, and $n_{E_g} = |E_g| = |P_g|$ is the number of skyrmions in that set. The parameter σ quantifies the uncertainty in the observed data O_g, and the use of $2\sigma^2$ in the denominator is explained in the discussion below. The loss $L_2(a,b)$ is averaged over time and measures the discrepancy between predicted and observed trajectories. In the special case–applicable to both of the studied examples–where n_{E_g} is independent of g, the quantity $L_2 \cdot \left(2\sigma^2/(n_g n_{E_g})\right)$ corresponds to the mean squared distance between the predicted and reference trajectories.

We interpret Equation 9 within the framework of maximum likelihood estimation. Assuming that the coordinate components are modeled as independent and identically distributed random variables, and that the errors are uncorrelated across different skyrmions, different trajectory sets, and distinct spatial components, but exhibit temporal correlation within the trajectory of a single skyrmion, the likelihood function $\mathscr{L}(a,b)$ is modeled in the following form:

$$\mathscr{L}(a,b) = p\left(\{(\vec{r}_{E_g,e}(t_{g,i}))_c\}_{i,c,e,g} \mid a,b\right) = \prod_{g,e,c} p_{g,e,c}\left(\{(\vec{r}_{E_g,e}(t_{g,i}))_c\}_i \mid a,b\right), \tag{10}$$

where the probability density is a modified Gaussian distribution,

$$p_{g,e,c}(\{x_i\}_i \mid a,b) \propto \exp\left(-\frac{1}{2\sigma^2} \left[\frac{1}{n_{t,g}} \sum_{i=1}^{n_{t,g}} \left(x_i - (\vec{r}_{P_g(a,b),e}(t_{g,i}))_c \right)^2 \right] \right). \tag{11}$$

Here, σ represents the expected standard deviation between the observed and predicted trajectories, accounting for errors, noise, tracking inaccuracies, and other uncertainties in the observed data. This formulation does not explicitly model the temporal structure of the data points within a trajectory. The quantity $\mathscr{L}(a,b)$ thus represents the likelihood of the observed data $\{(\vec{r}_{E_g,e}(t_{g,i}))_c\}_{i,c,e,g}$ given the model parameters a and b.

The maximum likelihood estimate is given by

$$(a^*,b^*) = \arg\max_{a,b} \mathscr{L}(a,b) = \arg\min_{a,b} (-\log \mathscr{L}(a,b)) = \arg\min_{a,b} L_2(a,b), \tag{12}$$

since $-\log \mathscr{L}(a,b)$ differs from $L_2(a,b)$ only by an additive constant, which has no effect on the optimization. This corresponds to the smallest discrepancy between the reference trajectories and the predicted ones generated using the parameters a^*, b^*. However, we use the posterior mean, as it incorporates the complete loss landscape. The posterior distribution $\pi(a,b)$, assuming flat priors over a and b, is given according to Bayes' theorem by

$$\pi(a,b) := p(a,b|\{(\vec{r}_{E_g,e}(t_{g,i}))_c\}_{i,c,e,g}) = \frac{\mathscr{L}(a,b)}{\int \mathrm{d}a\,\mathrm{d}b\,\mathscr{L}(a,b)}. \tag{13}$$

The optimal parameters are then calculated via the expectation value

$$\vec{X}^* = \begin{pmatrix} a^* \\ b^* \end{pmatrix} = \int_{\mathbb{R}^2} \mathrm{d}a\,\mathrm{d}b \begin{pmatrix} a \\ b \end{pmatrix} \pi(a,b). \tag{14}$$

In addition to identifying the optimal parameters a^* and b^*, one can also infer their associated uncertainties σ_{a^*} and σ_{b^*}. The covariance matrix $\mathrm{Cov}(\vec{X})$ of the parameter estimates $\vec{X} = (a,b)^T$ is given by

$$\mathbf{\Sigma} = \mathrm{Cov}(\vec{X}) = \int_{\mathbb{R}^2} \mathrm{d}a\,\mathrm{d}b \begin{pmatrix} (a-a^*)^2 & (a-a^*)(b-b^*) \\ (a-a^*)(b-b^*) & (b-b^*)^2 \end{pmatrix} \pi(a,b), \tag{15}$$

where the error of (a^*,b^*) is approximately Gaussian in the large-data limit. The standard deviations of the parameter estimates are then given by

$$\sigma_{a^*} = \sqrt{\mathbf{\Sigma}_{a,a}}, \qquad \sigma_{b^*} = \sqrt{\mathbf{\Sigma}_{b,b}}. \tag{16}$$

In this work, the inference was performed by evaluating $L_2(a,b)$ and $\pi(a,b)$ on a sufficiently dense mesh over a relevant rectangular region in the (a,b)-parameter space surrounding the minimum. This approach yields a loss landscape, from which the optimal parameters can be directly identified. Due to the ability to parallelize trajectory computations across a GPU, this strategy is computationally efficient. For each evaluation of $L_2(a,b)$ at a specific parameter pair (a,b), the predicted trajectories $\vec{r}_{P_g(a,b),i}(t)$ are first computed as described above, and then the loss is evaluated using Equation 9.

5.5 Remark

It should be noted that this approach can be extended to include more parameters or more complex functional forms of the force function $\vec{F}(\vec{r})$. The structure of the method remains unchanged and is applied analogously. Furthermore, it is also possible to model $\vec{F}(\vec{r})$ using a neural network, in which case the loss function in Equation 12 can be minimized iteratively using standard tools and optimization techniques commonly employed in training neural networks. In this case as well, the general procedure remains similar to what has been described here, and such neural network potential methods have already been used in various areas of physics and chemistry[14]. However, the method described here–based on only two parameters–is significantly less complex in terms of parameterization, as a small number of parameters is sufficient. This simplicity enables a complete and explicit characterization of the loss landscape and the direct estimation of parameter values and uncertainties.

6 Section B2: Estimation and inference of the skyrmion-skyrmion interaction potential from experimental and micromagnetic simulation data

Following the method described in the previous section, the skyrmion-skyrmion interaction potential is now determined both from the experimental trajectories and the micromagnetic simulations. The procedure for measuring the experimental data is described in the main text. Therefore, we first describe how the micromagnetic data were simulated, including the modeling of pinning effects. In both cases, when a current is applied, the skyrmions move toward or away from already pinned skyrmions. Since some skyrmions are pinned while others are mobile, their relative positions change under an applied current, depending on their local configuration. When the current is turned off, the skyrmions relax, but because their positions are slightly different, the trajectories of the relaxing skyrmions also differ slightly during the relaxation toward equilibrium positions. From these trajectories, the potential can be estimated and the error inferred using the method described above. Next, we compare the predicted trajectories with the trajectories used for parameter estimation, as well as the estimated skyrmion-skyrmion interaction potentials obtained from micromagnetic simulations and experiments.

6.1 Micromagnetic simulations

The micromagnetic parameters were chosen based on the stack also used in the experiment. As in the experiment, the following stack was used in the simulation: $[\mathrm{FM}(0.85\,\mathrm{nm})/\ \mathrm{NM}(1.4\,\mathrm{nm})/\ \mathrm{FM}(0.85\,\mathrm{nm})]_{25}$, where FM denotes a ferromagnetic layer and NM a non-magnetic layer. In the simulation, the bilayer $\mathrm{FM}(0.85\,\mathrm{nm})/\ \mathrm{NM}(1.4\,\mathrm{nm})/\ \mathrm{FM}(0.85\,\mathrm{nm})$ was modeled with periodic boundary conditions in the z-direction, with 12 repetitions on each side of the bilayer for the magnetostatic calculation.

For both FM layers, the experimentally measured values for the saturation magnetization $M_\mathrm{s} = 830 \times 10^3\,\mathrm{A\,m^{-1}}$ and the uniaxial magnetocrystalline anisotropy $K = 440 \times 10^3\,\mathrm{J\,m^{-3}}$ were used, with the easy axis given by $\vec{u} = \vec{e}_z$. The exchange stiffness was set to $A = 10\,\mathrm{pJ\,m^{-1}}$, which corresponds to the expected value for the experimental stack. The interfacial, isotropic Dzyaloshinskii–Moriya interaction (DMI) was adjusted to match the experimental energy minimum ε, yielding $\mathrm{DMI} = 0.84\,\mathrm{mJ\,m^{-2}}$, which is also in agreement with previous experiments. In the non-magnetic layer, the saturation magnetization was set to $M_\mathrm{s} = 0$. An interlayer exchange coupling of $J_\mathrm{IEC} = -0.45\,\mathrm{mJ\,m^{-2}}$ was introduced between the two FM layers. The Gilbert damping parameter was set to $\alpha = 0.1$, in accordance with the experimental measurements. As in the experiment, an external magnetic field of $B_z = 250\,\mathrm{mT}$ was applied. The simulations were performed using a modified version of MuMax3[15,16], which allows for uneven spacing in the z-direction and excludes the non-magnetic spacer region. As such, only the two $\mathrm{FM}(0.85\,\mathrm{nm})$ layers were simulated, using the corresponding computed demagnetizing kernel and an implementation of interlayer exchange coupling. The discretization in the x and y planes was set to $\Delta x = \Delta y = 2\,\mathrm{nm}$, and periodic boundary conditions were applied in both the x and y directions, as well as in the z direction, as described above.

First, the energy density ε at which the skyrmion lattice reaches its minimum energy was determined. A hexagonal

lattice was used for this purpose, as it has the highest packing density and is in agreement with the experiment. The periodicity P–i.e., the skyrmion–skyrmion distance–was varied. A rectangular simulation box with periodicity P, containing a rectangular unit cell with two skyrmions, was used, as shown in Figure S12**(b)**. The unit-cell area is $A_{\mathrm{uc}} = \sqrt{3}P^2$. An appropriate initial configuration was defined, consisting of cylindrical regions where the magnetization $m_z = \mp 1$ is opposite to the ferromagnetic background $m_z = \pm 1$. Opposite $m_z = \pm 1$ values were used for the ferromagnetic background in the two layers. Here, $\vec{m}$ denotes the reduced magnetization. This configuration was subsequently energy-minimized[17]. The total energy E_{tot} was calculated, and the energy density was obtained as $\varepsilon = \frac{E_{\mathrm{tot}}}{\sqrt{3}P^2}$. The dependence $\varepsilon(P)$ is shown in Figure S12 **(a)**. Since the lattice is expected to form at the lowest energy density, the equilibrium periodicity is given by $P^* = \arg\min_P \varepsilon(P)$. The minimum energy density in the simulation is at $P^* = 196\,\mathrm{nm}$, which agrees well with the experimentally observed periodicity and thus justifies the chosen value of the exchange stiffness.

Based on this, the dynamic simulation of the potential was performed. As an initial configuration, the unit cell with periodicity $P = 196\,\mathrm{nm}$ was used. This unit cell was repeated 3 times in the x- and 3 times in the y-direction, resulting in a simulation area of $[0\,\mathrm{nm}, 1020\,\mathrm{nm}] \times [0\,\mathrm{nm}, 588\,\mathrm{nm}]$, with periodic boundary conditions applied at the edges, see Figure S13 b). As in the energy minimization for the energy density, an initial configuration was set (the only difference being that multiple rectangular unit cells were used in the simulation area), and the energy was then minimized. To model pinning effects in the dynamic simulations, the regions U_2 and U_3 within the simulation area, see Figure S13, were fixed such that their magnetization remained unchanged throughout the simulation. In contrast, the region U_1 was not fixed. The skyrmions located in the central row R_1 are therefore completely free to move and scatter off the pinned skyrmions in the outer rows. At the left and right edges of the central vertical unit cell row, skyrmion rows R_2 and R_3 are present, extending across both the pinned and non-pinned regions. Specifically, one half of each of these boundary skyrmions lies within U_1 and is therefore unfixed, while the other half is located in U_2 or U_3 and is therefore fixed. This configuration reflects the physical situation in which pinning occurs within the domain wall, such that only one half of each boundary skyrmion is effectively pinned (namely, the half located in U_2 or U_3). The fixation was implemented by enforcing that no change in magnetization occurs within these regions, i.e., $\partial_t \vec{m} = 0$.

Starting from the minimized initial configuration consisting of the 3×3 rectangular unit cells, a spin-orbit torque was applied to drive the skyrmions, in close analogy to the experimental conditions. To this end, 10 simulations were performed with different current densities $\theta_{\mathrm{SH}} j = 0.75 \times 10^9\,\mathrm{A\,m^{-2}}$ to $2.25 \times 10^9\,\mathrm{A\,m^{-2}}$, which were chosen to be equally spaced over this range. Specifically, between $t = 0\,\mathrm{ns}$ and $t = 10\,\mathrm{ns}$, a current of the form $\theta_{\mathrm{SH}}\vec{j} = (j, 0, 0)$ (with $\theta_{\mathrm{SH}} > 0$) was applied. Afterward, the current was switched off, $\vec{j} = 0$, and the system was further evolved until $t = 20\,\mathrm{ns}$. At this point, all skyrmions have relaxed to their initial equilibrium state for the given material parameters. Depending on the applied current density, the maximum displacement of the skyrmions ranged from $10\,\mathrm{nm}$ to $40\,\mathrm{nm}$. The maximum current amplitude was chosen such that the resulting skyrmion displacement at the moment the current is turned off is approximately the maximum displacement observed experimentally. By performing simulations over a range of current densities, the

extraction of the effective potential becomes more accurate, as it is obtained from a variety of different trajectories. For symmetry reasons, $j_x < 0$ was not simulated, as it yields the same results as $j_x > 0$. The simulated dynamics for the different currents can also be seen in Supplementary Movie 5.

Due to the presence of pinned skyrmions, the relative distances between skyrmions deviate from the ideal lattice spacing P after the current is applied. When skyrmions are driven by spin–orbit torques, they interact with the pinned skyrmions, leading to irregular displacements within the skyrmion lattice. This results in modified forces and altered trajectories, from which the dynamics and the effective potential can be analyzed–as discussed at the beginning of this section.

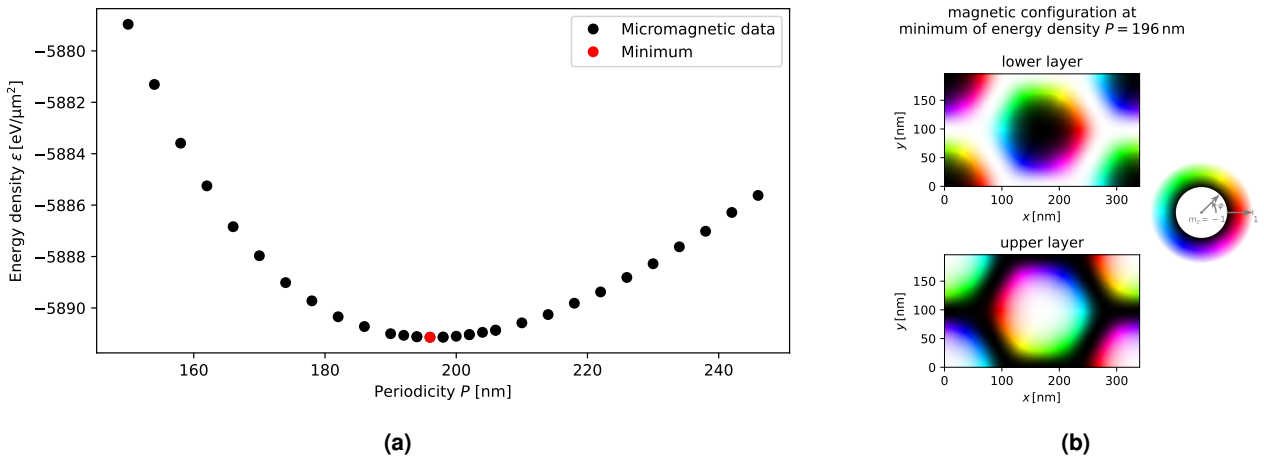

(a) **(b)**

Figure S12. (a) The energy density $\varepsilon(P) = \frac{E_{\text{tot}}}{\sqrt{3}P^2}$ for the skyrmion lattice phase calculated with micromagnetic simulations using the specified micromagnetic parameters given in the supplemental text. The resulting computed energy density is depicted by the black data points. The energy density minimum is located at $P = 196\,\text{nm}$. **(b)** On the right, the micromagnetic configuration at $P = 196\,\text{nm}$ is shown, corresponding to the minimum. The magnetization in both simulated layers is shown. A color wheel next to the plot indicates the direction of the magnetization.

6.2 Extraction and utilization of trajectory data

In the experimental data, m_z is known at every $1\,\mathrm{ns}$, allowing the trajectory $\vec{r}_{O_g,i}$ to be determined by tracking it using TrackMate, an extension for ImageJ[18]. The spatial resolution of m_z is $15\,\mathrm{nm}$.

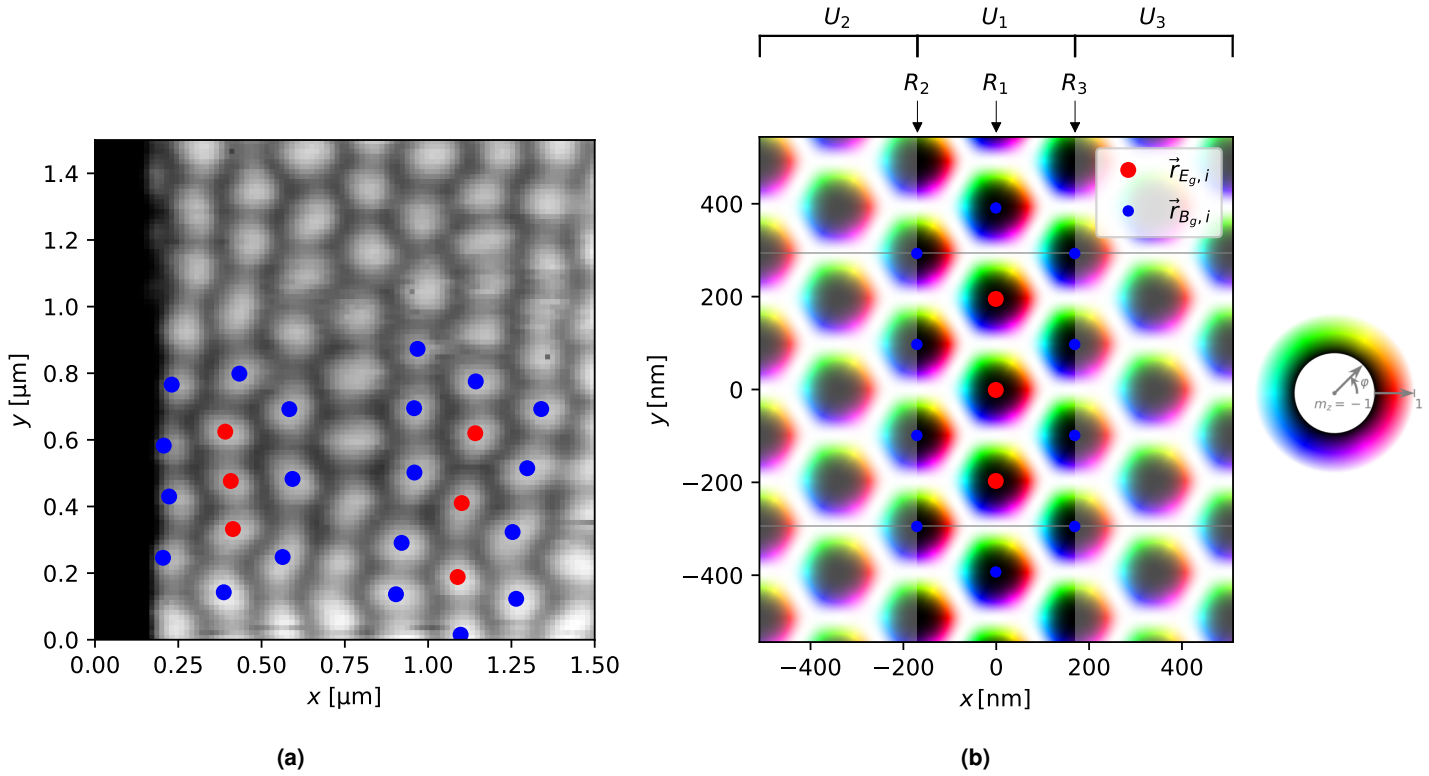

Figure S13. Plot of the skyrmions used to determine the skyrmion-skyrmion potential. In red are the positions of the skyrmions $\vec{r}_{E_g,i}$ at one time point, whose trajectories are used to estimate the skyrmion-skyrmion potential, and in blue are the boundary skyrmions $\vec{r}_{B_g,i}$, which are included for predicting the trajectories but whose own trajectories are not used. **(a)** Experimental case: in the background, the measured out-of-plane magnetization m_z, averaged over the time interval from $t = 650\,\mathrm{ns}$ to $t = 1400\,\mathrm{ns}$ (a period during which the skyrmions are relaxed). The skyrmion positions are also averaged over the same time window. **(b)** Magnetization from the micromagnetic simulation at $t = 0\,\mathrm{ns}$, corresponding to the equilibrium state. The magnetization direction is indicated by the color wheel. The region U_1 (consisting of the indicated vertical stripe) denotes the area where the magnetization is not fixed and evolves according to the LLG equation, while U_2 and U_3 (each consisting of one of the two indicated vertical stripes) denote the regions where the magnetization is fixed throughout the simulation. R_1, R_2, and R_3 denote the respective skyrmion rows. The skyrmion row R_1 is free, whereas R_2 and R_3 are half free and half pinned. The gray horizontal lines indicate the upper and lower boundaries of the simulation box; periodic repetitions of the simulation box are shown above and below. The white rectangles overlaid on the magnetization mark the regions where the magnetization was fixed throughout the simulation.

In the case of the micromagnetic data, the magnetization was recorded every $0.1\,\mathrm{ns}$. For each recorded time point, the magnetization state $\vec{m}$ was used to identify the skyrmion regions based on the condition $\frac{1}{2}\left((\vec{m}_\mathrm{L})_z(\vec{r}) - (\vec{m}_\mathrm{U})_z(\vec{r})\right) < 0$, where $\vec{m}_\mathrm{L}$ is the reduced magnetization in the lower layer and $\vec{m}_\mathrm{U}$ is the reduced magnetization in the upper layer of the bilayer. The connected regions identified by this condition correspond to individual skyrmions, for which the centroids were then calculated. Periodic boundary conditions were taken into account during this process. From the skyrmion positions at each time step, the trajectories were obtained by tracking them using the trackpy library[19].

For the experiment $n_g = 2$, i.e., two sets of trajectories: O_1 and O_2. These are defined as the time intervals following a current pulse ($j_x > 0$ or $j_x < 0$) until the next current pulse, during which the skyrmion lattice relaxes. Therefore, set O_1 corresponds to $t \in [452\,\mathrm{ns}, 1435\,\mathrm{ns}]$ and set O_2 to $t \in [1452\,\mathrm{ns}, 2000\,\mathrm{ns}] \cup [0\,\mathrm{ns}, 435\,\mathrm{ns}]$. In the simulation, we have $n_g = 10$, i.e., ten sets of trajectories O_g, corresponding to the ten different current densities used. For the micromagnetic simulations, in all sets O_g, the time interval considered is $t \in [10\,\mathrm{ns}, 20\,\mathrm{ns}]$, i.e., $t_{g,1} = 10\,\mathrm{ns}$ and $t_{g,2} = 20\,\mathrm{ns}$.

Based on this, the set O_g was divided into the set of trajectories used to estimate the potential, denoted E_g, and the set of boundary skyrmions, denoted B_g. In both experiment and simulation, boundary skyrmions were chosen as those that are pinned, since they cannot be included in E_g – their trajectories would need to be estimated, but the approach in Equation 3 would not be justified for this case. Furthermore, in the experiment, skyrmions that are located far from pinned skyrmions were also excluded from E_g, as they are not suitable for skyrmion-skyrmion interaction potential extraction either. Considering the above, the two sets were determined for both the experimental and the micromagnetic simulation data. See Figure S13, where the sets E_g and B_g are shown in red and blue, respectively. For the simulated case, $n_{E_g} = 3$, and for the experimental case, $n_{E_g} = 6$, see Figure S13. The boundary skyrmions B_g in the simulation that are periodic images–arising from the periodic boundary conditions–of skyrmions in E_g are treated straightforwardly as independent skyrmion quasi-particles. The trajectories from the set E_g for the experimental data are plotted in Figure S15, while the corresponding trajectories from the set E_g for the micromagnetic simulations are shown in Figure S16.

6.3 Loss evaluation, parameter estimation of (a^*, b^*), and inference of their uncertainty

With the experimentally and micromagnetically simulated trajectories, the skyrmion-skyrmion interaction potential can now be determined as described in section 5. For this purpose, only a segment of the trajectories of O_g, E_g, and B_g was considered, rather than their full length. This ensures that no excessive weight is assigned to the regime where the skyrmions are already relaxed and the interaction forces are weak due to the skyrmion lattice having relaxed over a longer timescale. This approach also helps to prevent overfitting. For the experimental trajectory, the time intervals considered are $t_{1,1} = 452\,\mathrm{ns}$ to $t_{1,2} = 552\,\mathrm{ns}$ and $t_{2,1} = 1452\,\mathrm{ns}$ to $t_{2,2} = 1552\,\mathrm{ns}$, resulting in a total of $n_{t,1} = n_{t,2} = 100$ data points, with a temporal resolution of $\delta t = 1\,\mathrm{ns}$. For the micromagnetically simulated trajectories, the considered time intervals are $t_{g,1} = 10\,\mathrm{ns}$ to $t_{g,2} = 20\,\mathrm{ns}$, yielding $n_{t,g} = 100$ data points for each current density, where a temporal resolution of $\delta t = 0.1\,\mathrm{ns}$ is used.

The resulting potential also works beyond the selected estimation intervals $[t_{g,1}, t_{g,2}]$, as confirmed by comparison with the full trajectories (see subsection 6.4). The number of optimization iterations for adjusting the initial configuration q_c was set to $q_c = 3$ for both the micromagnetic simulations and the experimental data.

Furthermore, the parameter σ, which accounts for errors, noise, tracking inaccuracies, uncertainties in the observed data, and uncertainties arising from the assumption that skyrmions can be approximated as quasiparticles following the Thiele equation, must be specified. Due to the centroid-based tracking approach used for the micromagnetic data, the skyrmion positions are determined with higher accuracy than the spatial resolution of the simulations. Therefore, σ

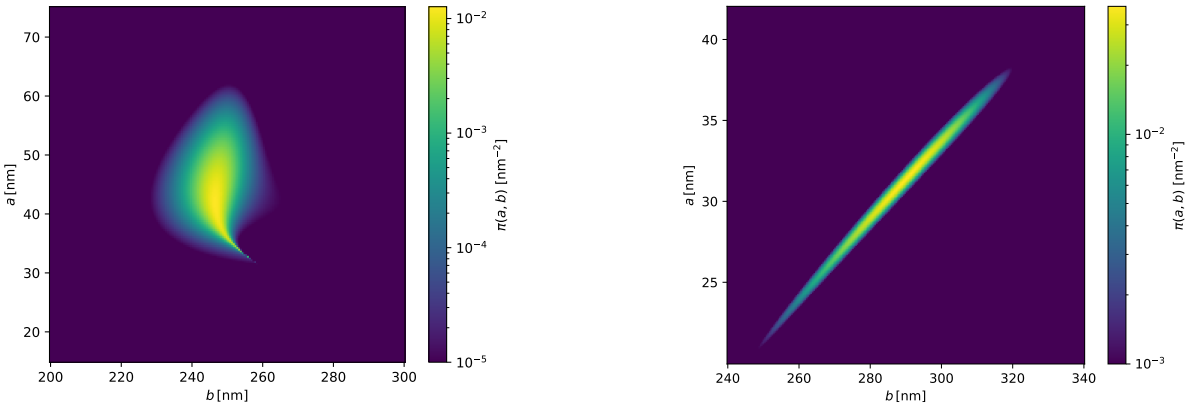

Figure S14. The posterior distribution $\pi(a,b)$ of the skyrmion interaction potential is computed at each parameter point (a,b) by comparing the trajectories obtained from experiments or micromagnetic simulations with those computed via time integration of the Thiele equation using the skyrmion-skyrmion interaction force $F_{(a,b)}(r)$. Posterior values in the color plot are capped at the minimum value shown in the color bar, with all lower values clipped to this threshold. **(a)** Posterior distribution $\pi(a,b)$ calculated from experiment. The resulting force parameters are $a^* = 44\,\mathrm{nm}$ and $b^* = 247\,\mathrm{nm}$. **(b)** Posterior distribution $\pi(a,b)$ calculated from the micromagnetic simulation. The resulting force parameters are found to be $a^* = 31\,\mathrm{nm}$ and $b^* = 288\,\mathrm{nm}$.

was set to half the respective spatial discretization in the micromagnetic simulation ($\sigma = 1\,\mathrm{nm}$) and in the experiment ($\sigma = 7.5\,\mathrm{nm}$). This value of σ also reflects the approximation that skyrmions can be treated as quasi-particles.

The quantity $L_2(a,b)$ was determined as described in section 5. This yields the posterior distribution $\pi(a,b)$, as shown in Figure S14. From this, the optimal parameters (a^*,b^*) (see Equation 14) are determined, along with their associated uncertainties, quantified by the covariance matrix $\mathbf{\Sigma}$ and the standard deviations σ_{a^*} and σ_{b^*} (see Equation 15), resulting in:

	Experiment	Micromagnetic simulation
$a^*\,[\mathrm{nm}]$	44	31
$b^*\,[\mathrm{nm}]$	247	288
$\mathbf{\Sigma} = \mathrm{Cov}(\vec{X})\,[\mathrm{nm}^2]$	$\begin{pmatrix} 20 & 0.8 \\ 0.8 & 14 \end{pmatrix}$	$\begin{pmatrix} 10 & 42 \\ 42 & 176 \end{pmatrix}$
$\sigma_{a^*}\,[\mathrm{nm}]$	4	3
$\sigma_{b^*}\,[\mathrm{nm}]$	4	13

Table 2. Optimal parameters (a^*,b^*) estimated from experimental data and micromagnetic simulations. The associated uncertainties are quantified by the covariance matrix $\mathbf{\Sigma}$ and the corresponding standard deviations σ_{a^*} and σ_{b^*}.

Thus, the parameters (a^*,b^*) with their associated uncertainties are inferred.

6.4 Comparison between predicted trajectories and trajectories used for estimation

Based on the determined parameters a^* and b^*, the trajectories $\vec{r}_{P_g(a^*,b^*),i}$ can now be computed for both the experimental case and the micromagnetic simulation, using subsection 5.3. As initial positions, those obtained during the estimation procedure were used (see Equation 8). Time integration was carried out up to the point where the full trajectory data is available, extending beyond the estimation interval $[t_{g,1}, t_{g,2}]$. The results are shown in Figure S15 for the experiment and in Figure S16 for the micromagnetic simulation. It can be observed that the predicted trajectories match with the data even beyond the time window used for estimation, for all skyrmions and currents. The following holds for both cases:

	Micromagnetic simulation	Experiment
$\mathrm{avg}(\{\lvert \left(\vec{r}_{P_g(a^*,b^*),i}\right)_c(t) - \left(\vec{r}_{E_g,i}\right)_c(t)\rvert\}_{t,g,i,c})$	$< 0.5\,\mathrm{nm}$	$\leq 12\,\mathrm{nm}$

Table 3. Average absolute deviation between predicted trajectories $\vec{r}_{P_g(a^*,b^*)}$ and observed trajectories $\vec{r}_{E_g}$, evaluated over all times t, skyrmions i, currents g, and spatial components c. Results are shown for micromagnetic simulations and experimental data.

where $\mathrm{avg}(X) = \frac{1}{|X|}\sum_{x\in X} x$ denotes the average of all elements in the set. Therefore, in both the experimental and micromagnetic simulation cases, the deviation is less than or on the order of σ. In the experimental case, the error is slightly larger than σ, as tracking is more ambiguous due to slight deformations of the skyrmions and uncertainties in determining the centroid. These errors differ for each skyrmion but remain approximately constant over time for each relaxation. It follows that the trajectories $\vec{r}_{P_g(a^*,b^*),i}$ agree with the original trajectories $\vec{r}_{E_g,i}$ for both the experimental and the micromagnetic simulation cases.

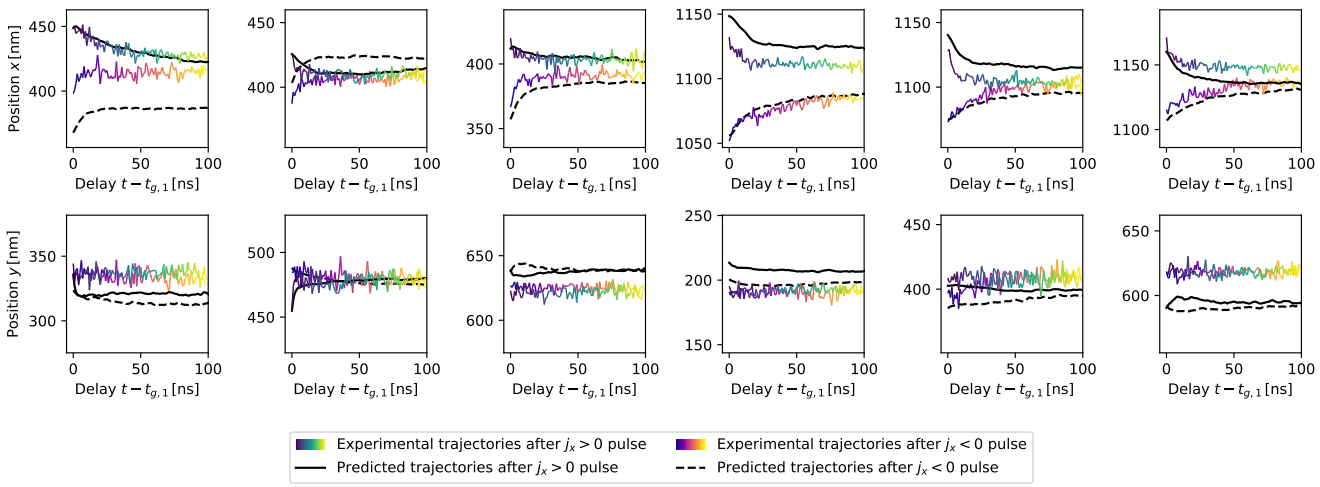

Figure S15. Plot of the experimental trajectories $\vec{r}_{E_g,i}(t)$ (depicted with a color gradient), which were used to estimate the potential parameters, and the predicted trajectories $\vec{r}_{P_g(a^*,b^*),i}(t)$ (shown in green), obtained by numerically integrating the Thiele equation using the optimal parameters (a^*, b^*) for the experiment. The potential was estimated from skyrmion relaxation trajectories under the application of current densities $+j_x$ and $-j_x$ (with $j_x > 0$). For each skyrmion, both relaxation trajectories corresponding to $\pm j$ are displayed in a single subplot. The x- and y-coordinates of these trajectories are plotted over delay time $t - t_{g,1}$, with the starting times of both relaxations from the two sets shifted so that the starting points of the relaxations coincide. These six examples correspond to the six red-highlighted skyrmions shown in Figure S13 **(a)**. Due to noise in the experimental trajectories of boundary skyrmions, denoted $\vec{r}_{B_g,i}(t)$, the corresponding predicted trajectories are also influenced by this noise.

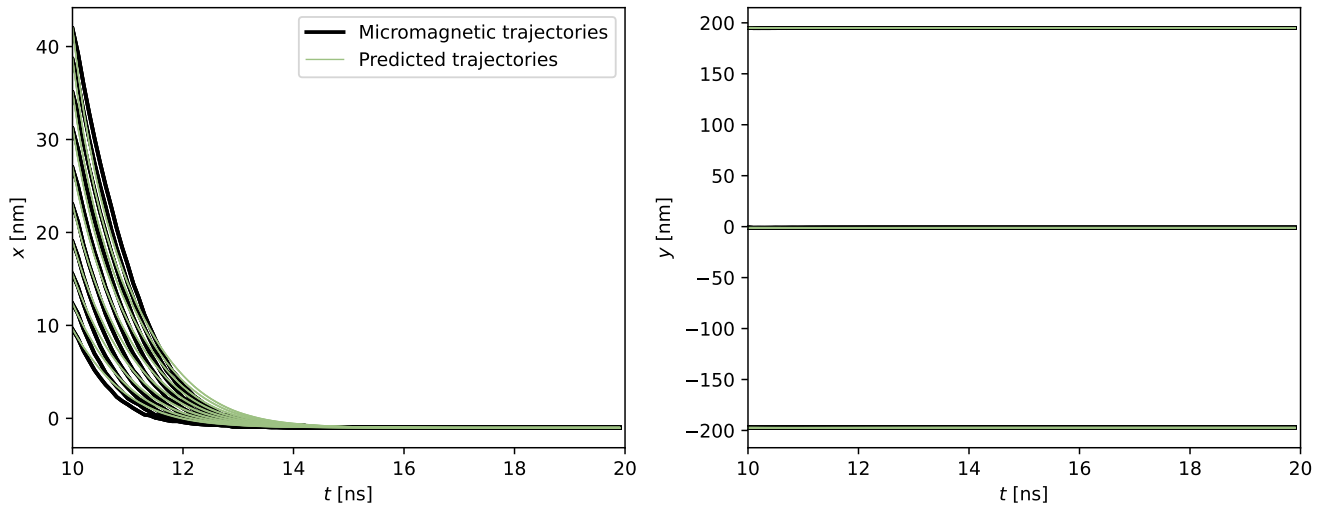

Figure S16. Comparison between the trajectories obtained from micromagnetic simulations $\vec{r}_{E_g,i}(t)$ (black) and the predicted trajectories $\vec{r}_{P_g(a,b),i}(t)$ (green), computed via time integration of the Thiele equation using the optimal parameters (a^*, b^*) for the micromagnetic data. In total, 30 relaxation trajectories are shown, corresponding to the three red-highlighted skyrmions in Figure S13 **(b)** for the ten different current densities. The potential was estimated from relaxation trajectories under applied current densities $j_x > 0$. Due to the regular lattice arrangement, multiple skyrmions share identical or similar x-coordinates, leading to overlapping trajectories in the plots. There is good agreement between the micromagnetic (black) and Thiele-predicted (green) trajectories. Two subplots are used to display the x- and y-components of the positions as functions of time.

6.5 Comparison of estimated skyrmion-skyrmion interaction potentials

After estimating the parameters a^* and b^* and validating the predicted trajectories $\vec{r}_{P_g(a^*,b^*),i}$, the skyrmion-skyrmion interaction potential $V_{(a^*,b^*)}(r)$ can now be compared between the experimental data and the micromagnetic simulation, using the expression given in Equation 2. To compute $V_{(a^*,b^*)}(r)$, the dissipation constant D was calculated from the dissipation tensor $\mathscr{D}$[12], which, in the case of rotationally symmetric skyrmions, as is the case in our system, is given by

$$D = \frac{\mathscr{D}_{xx} + \mathscr{D}_{yy}}{2} = \mathscr{D}_{xx} = \mathscr{D}_{yy}, \quad \mathscr{D}_{xy} = 0, \quad \text{with} \quad \mathscr{D}_{ij} = \frac{\alpha M_s h}{\gamma} \int_{\Omega_S} \mathrm{d}^2\vec{r}\, \frac{\partial \vec{m}}{\partial x_j} \cdot \frac{\partial \vec{m}}{\partial x_i}, \tag{17}$$

where Ω_S is the domain of a single skyrmion and h is the height of the ferromagnetic film. This value was computed from the same micromagnetic simulations used for the dynamical simulations. The dissipation tensor from Equation 17 was evaluated over the entire simulation domain (i.e., in Equation 17, Ω_S was replaced by the full simulation domain) and then divided by the number of skyrmions. The dissipation constant remains approximately constant throughout the dynamic simulation. The resulting dissipation constant is $D = N\,0.27\,\mathrm{meV\,s\,m^{-1}\,nm^{-1}}$, where $N = 25$ is the number of repetitions, and $0.27\,\mathrm{meV\,s\,m^{-1}\,nm^{-1}}$ is the value obtained by integrating over the two simulated layers (which have periodic boundary conditions in the z-direction). Note that the quantity V/D is independent of the number of repetitions in synthetic antiferromagnets. This is because $V_{(a^*,b^*)}$ increases approximately linearly with the number of repetitions, especially for $N \gg 1$. In antiferromagnetic stacking, dipolar fields largely cancel, leading to a dipolar energy that scales linearly, while the remaining energy contributions also scale linearly with N. Similarly, the dissipation constant D increases linearly with the number of repetitions. Therefore, the ratio V/D remains independent of N. Using this value in Equation 2, we obtain the skyrmion–skyrmion interaction potential for the simulation, $V_{(a^*,b^*)}$, see the upper plot in Figure S17.

In general dissipation constants D determined from experiments are systematically larger compared to the theory without inhomogeneities, which is generally attributed to nanoscale roughness[20–22]. Accordingly, we introduce a phenomenological scaling factor, leading to

$$D = \eta \frac{\mathscr{D}_{xx} + \mathscr{D}_{yy}}{2}, \tag{18}$$

with $\eta \geq 1$. The factor η indicates how much the effective dissipation constant in the experiment exceeds the value predicted by the theory without inhomogeneities. Consequently, the force parameter b likewise exhibits a discrepancy compared to a theory without inhomogeneities. This behavior follows from

$$F(r) = 1\,\mathrm{m\,s^{-1}} \underbrace{\left[\eta \mathscr{D}_{xx} \exp\left(\frac{b}{a}\right)\right]}_{C} \exp\left(-\frac{r}{a}\right), \tag{19}$$

where C denotes the prefactor (i.e., the amplitude) of the potential, while the spatial dependence of the force is exclusively determined by the exponential term $\exp(-r/a)$. Consequently, the parameter a remains independent of the specific value

of η within the potential extraction procedure. By comparing $\vec{F}_{(a^*,b^*)}(\vec{r}) = -\nabla_{\vec{r}} V_{(a^*,b^*)}(|\vec{r}|)$ (with $V_{(a^*,b^*)}(|\vec{r}|)/D$ given in Equation 2) over the experimentally relevant range of r to the corresponding simulations, we deduce $\eta \approx 4$. Consequently, for the experimental system, we obtain $D = N\,1.08\,\mathrm{meV\,s\,m^{-1}\,nm^{-1}}$. The fact that the dissipation constant is different can also be seen from the timescale of the relaxation: after displacement, the timescale is longer in the experiment than in the simulation. This ultimately yields the experimentally determined skyrmion-skyrmion interaction potential, as presented in Figure S17.

In addition to the potential $V_{(a^*,b^*)}(r)$, the corresponding uncertainty band is shown in Figure S17 for both the micromagnetic and experimental cases. To determine the uncertainty band, the following approach was used: since the uncertainty of (a^*,b^*) is described by a multivariate normal distribution (see Equation 15) and the covariance matrix $\mathbf{\Sigma}$ has been estimated, the uncertainty band can be computed via Monte Carlo sampling. Specifically, $V_{(a,b)}(r)$ is repeatedly calculated by sampling (a,b) from a multivariate normal distribution with mean (a^*,b^*) and covariance matrix $\mathbf{\Sigma}$. The uncertainty band is then defined by the 16th and 84th percentiles of the determined potentials, which corresponds approximately to a 68% confidence interval, i.e., one standard deviation of $V(r)$. Within these error bands, there is good agreement between the theoretical and experimental skyrmion-skyrmion interaction potentials $V_{(a^*,b^*)}(r)$. Even without the uncertainty bands, the potential curves from experiment and simulation closely match. In the lower plot of Figure S17, the histogram of pairwise skyrmion distances is shown for the set $\left\{|\vec{r}_{E_g,i} - \vec{r}_{E_g,j}|\right\}_{i\neq j,g} \cup \left\{|\vec{r}_{E_g,i} - \vec{r}_{B_g,j}|\right\}_{i,j,g}$, which includes all inter-skyrmion distances used for the estimation of the optimal interaction parameters a^* and b^*.

These uncertainty bands are shown for both the experimental and micromagnetic cases. Note that Figure S17 is identical to Fig. 3 in the main text and is included here to accompany the step-by-step procedure described in Supplementary section B.

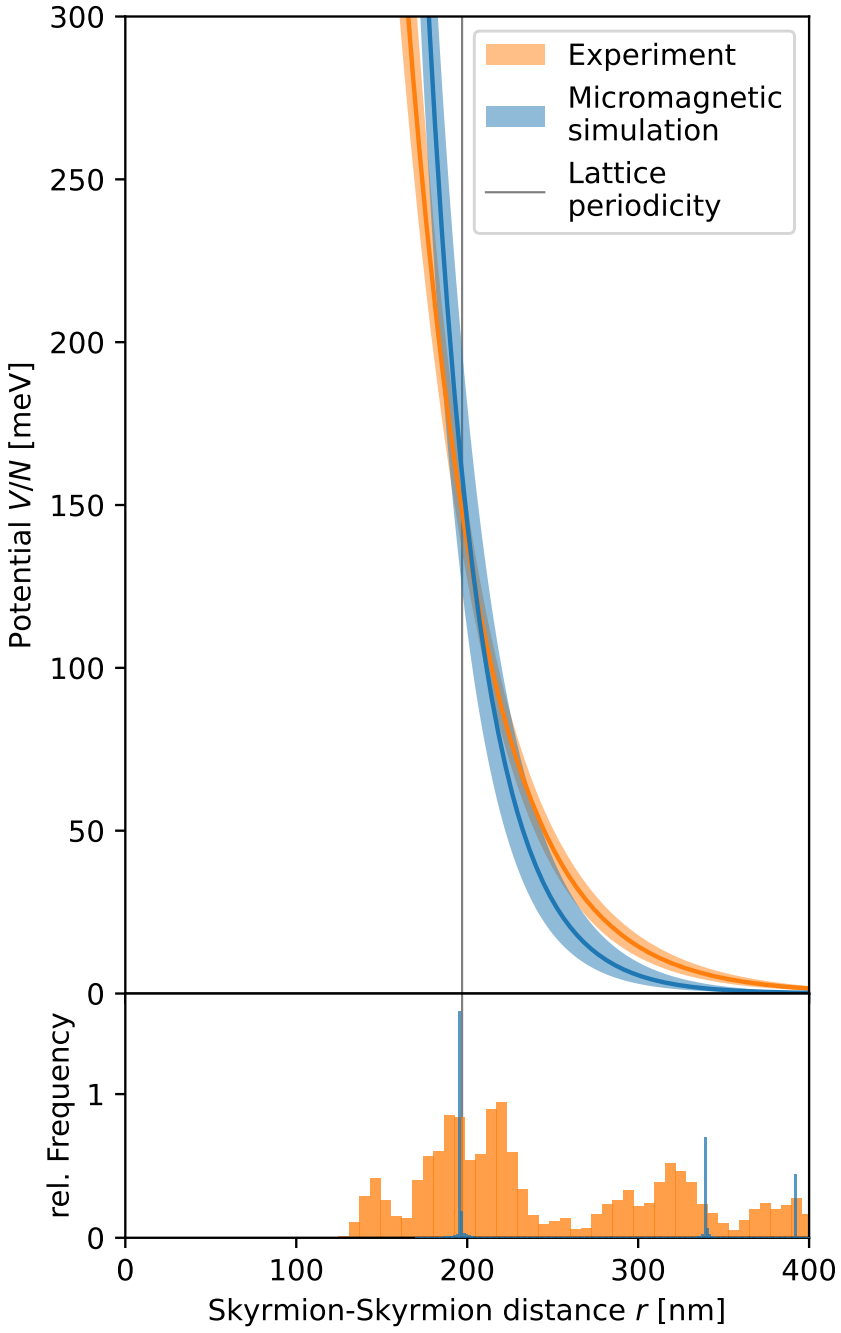

Figure S17. Skyrmion–skyrmion interaction potential for experiment and simulation. The upper plot compares the skyrmion-skyrmion interaction potentials per bilayer repetition, $V_{(a^*,b^*)}(|\vec{r}|)/N$, obtained from experimental data (orange) and micromagnetic simulations (blue), as a function of the distance r. The shaded regions, colored to match their respective curves, indicate 68% uncertainty bands. In the lower plot, a histogram is shown of all pairwise skyrmion distances used for the estimation of the optimal interaction parameters a^* and b^*, for both the experimental and simulation data. Additionally, the thin vertical line indicates the periodicity of the lattice $P^* = 196\,\mathrm{nm}$. The skyrmion–skyrmion interaction force is obtained from the potential as $\vec{F}_{(a^*,b^*)}(\vec{r}) = -\nabla_{\vec{r}} V_{(a^*,b^*)}(|\vec{r}|)$.

6.6 Interaction potential in dependence of micromagnetic parameters and density

As a next step, we investigated how the potential parameters a and b depend on variations in the material parameters exchange stiffness (A), DMI (DMI), saturation magnetization (M_s), anisotropy (K), and external magnetic field (B_z), as well as on the skyrmion density $\rho = 2A_\mathrm{uc}^{-1} = 2(\sqrt{3}P^2)^{-1}$. The reference parameter set corresponds to the experimental conditions described in subsection 6.1.

To isolate the influence of each material parameter, we varied one parameter at a time while keeping all others fixed at their reference values. For each parameter, a total of several values were considered, distributed above and below the reference value, resulting in several distinct material parameter sets per parameter, in which only the respective parameter is varied while all others remain fixed at their reference values. The upper and lower bounds of this variation were chosen based on physically reasonable and relevant parameter ranges and the requirement that the optimal periodicity, i.e., the minimum of the energy density, remains below $300\,\mathrm{nm}$. For each of these parameter sets, the periodicity P was varied in the range from $100\,\mathrm{nm}$ to $310\,\mathrm{nm}$ in steps of $10\,\mathrm{nm}$. The corresponding energy density $\varepsilon(P)$ was computed, and the optimal periodicity $P^* = \arg\min_P \varepsilon(P)$ was determined via a quadratic fit using the three values around the minimum, i.e., the minimum value and its immediate left and right neighbors. Using the optimal periodicity P^* for each material parameter set, scattering simulations were performed for 10 different current densities. Subsequently, the potential parameters a^* and b^* were extracted for each case following the procedure described previously. In this way, the potential is obtained as a function of the underlying material parameters. The resulting quantities–namely P^*, a^*, b^*, and $V(r)$–as functions of the respective varied parameter are presented in the following figures: Figure S18 for the exchange stiffness A, Figure S19 for the DMI interaction strength DMI, Figure S20 for the saturation magnetization M_s, Figure S21 for the uniaxial anisotropy K, and Figure S22 for the external magnetic field B_z.

Additionally, we considered the reference parameter set without modifying any of the magnetic material parameters and varied only the skyrmion density $\rho(P) = 2(\sqrt{3}P^2)^{-1}$. In this case, the energy density is not minimized; instead, the periodicity $P = (\sqrt{3}\rho/2)^{-1/2}$ is directly determined by the chosen density. Analogously to the variation of the magnetic material parameters, for each density and the corresponding periodicity P, 10 scattering simulations were performed, and the potential parameters were subsequently extracted. The resulting quantities P, a^*, b^*, and $V(r)$ as functions of the skyrmion density are shown in Figure S23.

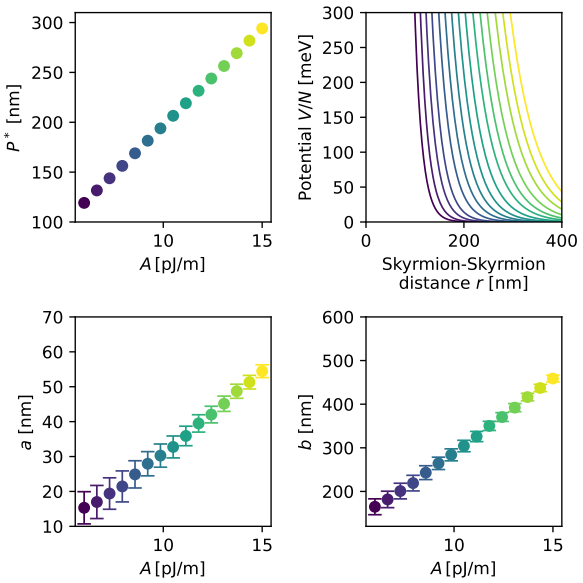

Figure S18. Dependence of skyrmion-skyrmion interaction potential parameters a and b on the exchange stiffness A. Upper left: Dependence of the periodicity minimum of the energy density, $P^* = \arg\min_P \varepsilon(P)$, on variations of the exchange stiffness. The color indicates the value of the exchange stiffness and is used consistently across all plots. Lower panels: Dependence of the potential parameters a and b on the exchange stiffness, where, for each respective value, the periodicity corresponding to the minimum of the energy density is used. Error bars denote the standard deviations of the inferred potential parameters a^* and b^*. Upper right: Resulting skyrmion-skyrmion interaction potential per bilayer $V(r)/N$ as a function of the skyrmion-skyrmion distance r.

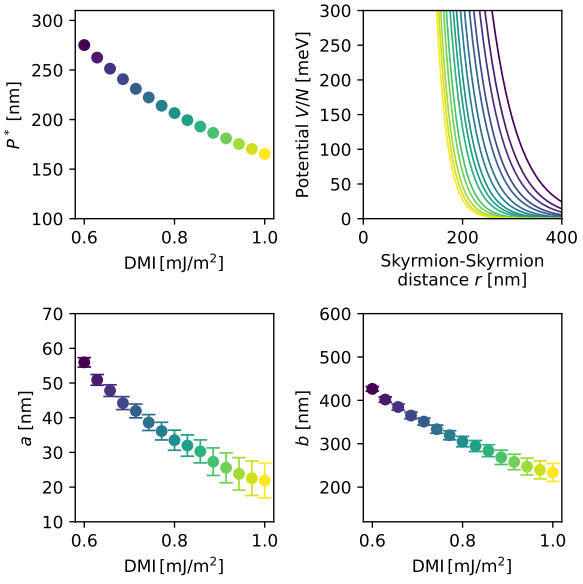

Figure S19. Dependence of the skyrmion-skyrmion interaction potential parameters a and b on the DMI interaction strength DMI. Upper left: Dependence of the periodicity minimum of the energy density, $P^* = \arg\min_P \varepsilon(P)$, on variations of the DMI interaction strength. The color indicates the value of the DMI interaction strength and is used consistently across all plots. Lower panels: Dependence of the potential parameters a and b on the DMI interaction strength, where, for each respective value, the periodicity corresponding to the minimum of the energy density is used. Error bars denote the standard deviations of the inferred potential parameters a^* and b^*. Upper right: Resulting skyrmion-skyrmion interaction potential per bilayer $V(r)/N$ as a function of the skyrmion-skyrmion distance r.

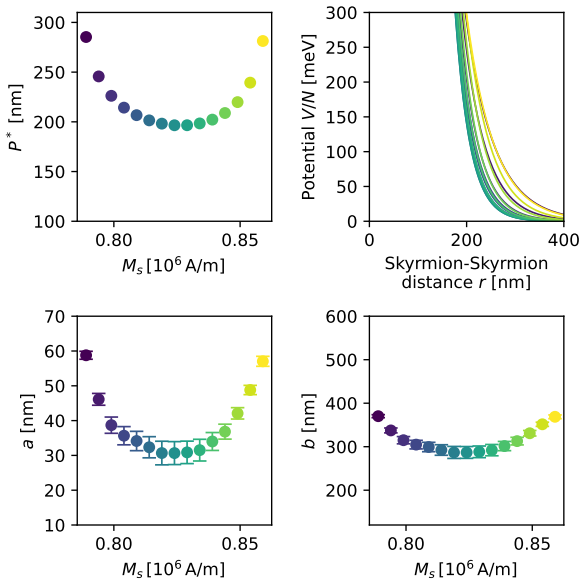

Figure S20. Dependence of the skyrmion-skyrmion interaction potential parameters a and b on the saturation magnetization M_s. Upper left: Dependence of the periodicity minimum of the energy density, $P^* = \arg\min_P \varepsilon(P)$, on variations of the saturation magnetization. The color indicates the value of the saturation magnetization and is used consistently across all plots. Lower panels: Dependence of the potential parameters a and b on the saturation magnetization, where, for each respective value, the periodicity corresponding to the minimum of the energy density is used. Error bars denote the standard deviations of the inferred potential parameters a^* and b^*. Upper right: Resulting skyrmion-skyrmion interaction potential per bilayer $V(r)/N$ as a function of the skyrmion-skyrmion distance r.

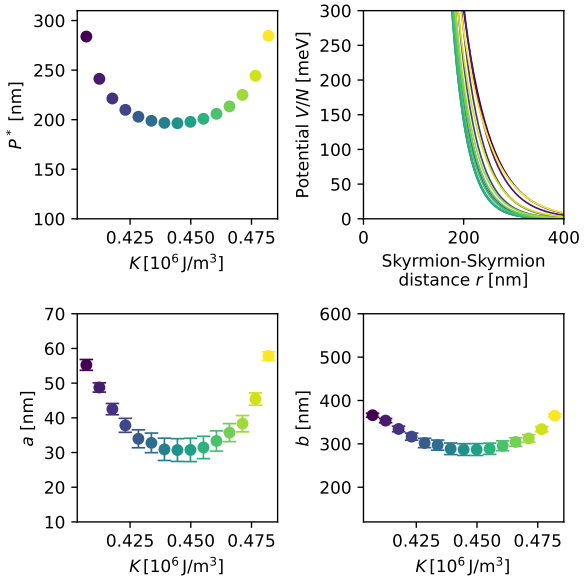

Figure S21. Dependence of the skyrmion-skyrmion interaction potential parameters a and b on the uniaxial anisotropy K. Upper left: Dependence of the periodicity minimum of the energy density, $P^* = \arg\min_P \varepsilon(P)$, on variations of the uniaxial anisotropy. The color indicates the value of the uniaxial anisotropy and is used consistently across all plots. Lower panels: Dependence of the potential parameters a and b on the uniaxial anisotropy, where, for each respective value, the periodicity corresponding to the minimum of the energy density is used. Error bars denote the standard deviations of the inferred potential parameters a^* and b^*. Upper right: Resulting skyrmion-skyrmion interaction potential per bilayer $V(r)/N$ as a function of the skyrmion-skyrmion distance r.

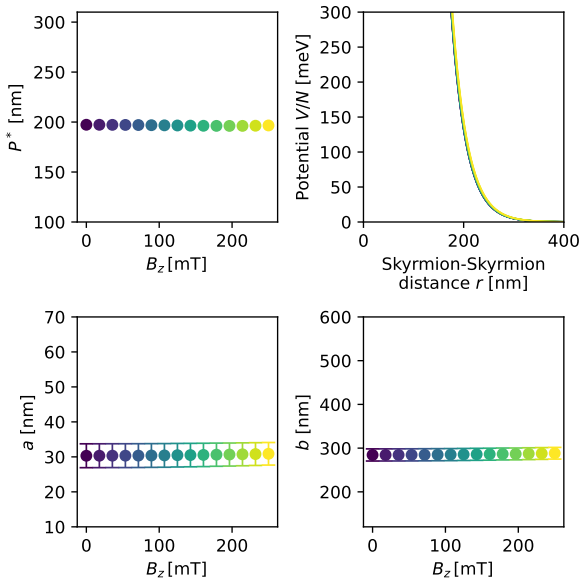

Figure S22. Dependence of the skyrmion-skyrmion interaction potential parameters a and b on the external field B_z. Upper left: Dependence of the periodicity minimum of the energy density, $P^* = \arg\min_P \varepsilon(P)$, on variations of the external field. The color indicates the value of the external field and is used consistently across all plots. Lower panels: Dependence of the potential parameters a^* and b^* on the external field, where, for each respective value, the periodicity corresponding to the minimum of the energy density is used. Error bars denote the standard deviations of the inferred potential parameters a^* and b^*. Upper right: Resulting skyrmion-skyrmion interaction potential per bilayer $V(r)/N$ as a function of the skyrmion-skyrmion distance r.

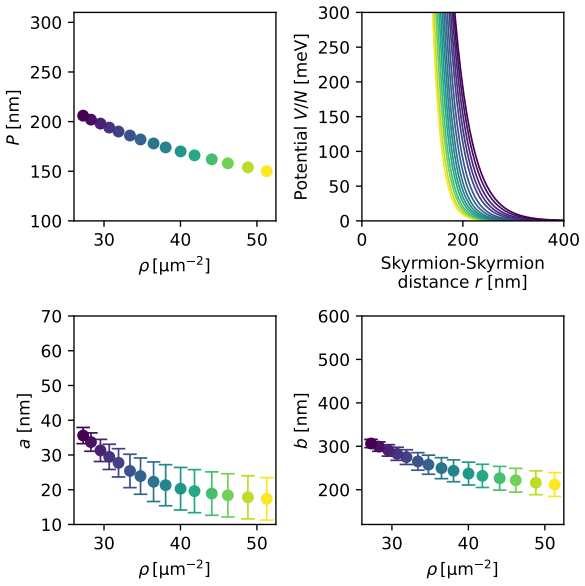

Figure S23. Dependence of the skyrmion-skyrmion interaction potential parameters a and b on the density ρ. Upper left: Dependence of the skyrmion density $\rho = 2/(\sqrt{3}P^2)$ of the hexagonal skyrmion lattice on variations of the periodicity P, while all other material parameters are kept constant. The color indicates the value of the density and is used consistently across all plots. Lower panels: Dependence of the potential parameters a^* and b^* on the density, where, for each respective value, the periodicity $P = (\sqrt{3}\rho/2)^{-1/2}$ is used. Error bars denote the standard deviations of the inferred potential parameters a^* and b^*. Upper right: Resulting skyrmion-skyrmion interaction potential per bilayer $V(r)/N$ as a function of the skyrmion-skyrmion distance r.

7 Supplementary Videos

Supplementary Video 1

Time-resolved STXM movie showing the current-driven incoherent dynamics of the antiferromagnetic skyrmion lattice imaged in sublattice A.

Supplementary Video 2

Time-resolved STXM movie showing the current-driven incoherent dynamics of the antiferromagnetic skyrmion lattice imaged in sublattice B.

Supplementary Video 3

Time-resolved STXM movie showing coherent viscous flow of the antiferromagnetic skyrmion lattice in sublattice A at higher current density.

Supplementary Video 4

Time-resolved STXM movie showing the current-driven motion of non-interacting antiferromagnetic skyrmions.

Supplementary Video 5

Micromagnetic simulation movie showing the current-driven interaction and subsequent relaxation of free antiferromagnetic skyrmions with pinned skyrmions at different current densities.

References

1. Song, D. *et al.* Steady motion of 80-nm-size skyrmions in a 100-nm-wide track. *Nat. Commun.* **15**, 5614 (2024).

2. Peng, L. *et al.* Dynamic transition of current-driven single-skyrmion motion in a room-temperature chiral-lattice magnet. *Nat. Commun.* **12**, 6797 (2021).

3. Dohi, T., DuttaGupta, S., Fukami, S. & Ohno, H. Formation and current-induced motion of synthetic antiferromagnetic skyrmion bubbles. *Nat. Commun.* **10**, 1–6 (2019).

4. Pham, V. T. *et al.* Fast current-induced skyrmion motion in synthetic antiferromagnets. *Science* **384**, 307–312, DOI: 10.1126/science.add5751 (2024).

5. Dohi, T. *et al.* Observation of a non-reciprocal skyrmion hall effect of hybrid chiral skyrmion tubes in synthetic antiferromagnetic multilayers. *Nat. Commun.* **16**, 8285 (2025).

6. Woo, S. *et al.* Observation of room-temperature magnetic skyrmions and their current-driven dynamics in ultrathin metallic ferromagnets. *Nat. Mater.* **15**, 501–506 (2016).

7. Lemesh, I. *et al.* Current-induced skyrmion generation through morphological thermal transitions in chiral ferromagnetic heterostructures. *Adv. Mater.* **30**, 1805461 (2018).

8. Litzius, K. *et al.* The role of temperature and drive current in skyrmion dynamics. *Nat. Electron.* **3**, 30–36 (2020).

9. Birch, M. *et al.* Toggle-like current-induced bloch point dynamics of 3d skyrmion strings in a room temperature nanowire. *Nat. Commun.* **13**, 3630 (2022).

10. Schäffer, A. F., Rózsa, L., Berakdar, J., Vedmedenko, E. Y. & Wiesendanger, R. Stochastic dynamics and pattern formation of geometrically confined skyrmions. *Commun. Phys.* **2**, 72 (2019).

11. Ge, Y. *et al.* Constructing coarse-grained skyrmion potentials from experimental data with iterative boltzmann inversion. *Commun. Phys.* **6**, 30, DOI: 10.1038/s42005-023-01145-9 (2023).

12. Thiele, A. A. Steady-state motion of magnetic domains. *Phys. Rev. Lett.* **30**, 230–233 (1973).

13. Msiska, R., Rodrigues, D. R., Leliaert, J. & Everschor-Sitte, K. Nonzero skyrmion hall effect in topologically trivial structures. *Phys. Rev. Appl.* **17** (2022).

14. Kocer, E., Ko, T. W. & Behler, J. Neural network potentials: A concise overview of methods. *Annu. Rev. Phys. Chem.* **73**, 163–186 (2022).

15. Vansteenkiste, A. *et al.* The design and verification of Mumax3. *AIP Adv.* **4**, 107133 (2014).

16. Mulkers, J., Van Waeyenberge, B. & Milošević, M. V. Effects of spatially-engineered Dzyaloshinskii-Moriya interaction in ferromagnetic films. *Phys. Rev. B.* **95**, 144401 (2017).

17. Exl, L. *et al.* LaBonte's method revisited: An effective steepest descent method for micromagnetic energy minimization. *J. Appl. Phys.* **115**, 17D118 (2014).

18. Ershov, D. *et al.* Trackmate 7: integrating state-of-the-art segmentation algorithms into tracking pipelines. *Nat. Methods* **19**, 829–832 (2022).

19. Allan, D. B., Caswell, T., Keim, N. C., van der Wel, C. M. & Verweij, R. W. soft-matter/trackpy: v0.7 (2025).

20. Zázvorka, J. *et al.* Thermal skyrmion diffusion used in a reshuffler device. *Nat. Nanotechnol.* **14**, 658–661 (2019).

21. Reichhardt, C., Reichhardt, C. J. O. & Milošević, M. Statics and dynamics of skyrmions interacting with disorder and nanostructures. *Rev. Mod. Phys.* **94**, 035005 (2022).

22. Brems, M. A. *et al.* Realizing quantitative quasiparticle modeling of skyrmion dynamics in arbitrary potentials. *Phys. Rev. Lett.* **134**, 046701 (2025).